TÉCNICO LISBOA

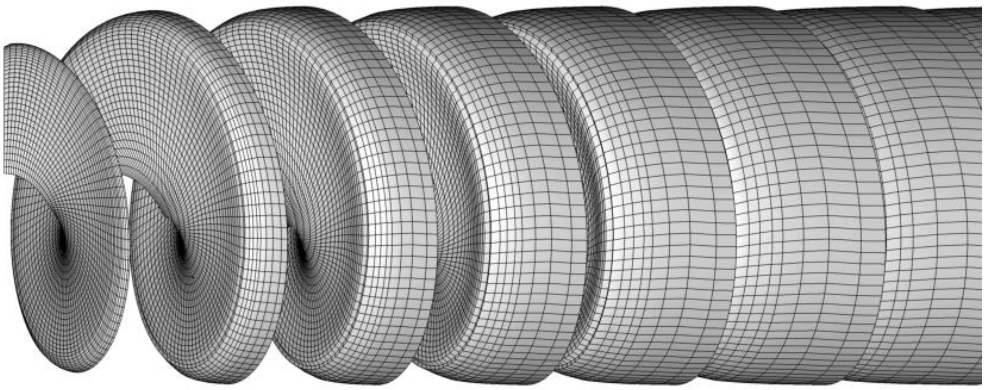

Effects of expansion in the wake alignment of horizontal axis turbines with a lifting line model

Marcin Dolata

Thesis to obtain the Master of Science Degree in

Energy Engineering and Management

Supervisors: Prof. José Alberto Caiado Falcão de Campos
Dr. João Manuel Ribeiro da Costa Baltazar

Examination Committee

President: Prof. Edgar Caetano Fernandes
Supervisor: Prof. José Alberto Caiado Falcão de Campos
Member of the Committee: Prof. Luís Manuel de Carvalho Gato

January 2021

Acknowledgments

First and foremost, I want to thank my family, especially Parents – Renata and Arkadiusz Dolata – for supporting me, being patient and ever so understanding with the amount of time and attention I had to devote to my studies. I am truly hopeful that I will have an opportunity to repay for their kindness and patience in the future.

Afterwards, I would like to thank my two thesis supervisors, Professors José Falcão de Campos and João Baltazar for providing me with highly helpful advices, aiding me with their expert-level knowledge and motivating me when I doubted myself. I truly appreciate having an opportunity of immersing myself into such an interesting subject.

Lastly, I must express my gratitude to my friends – Madzia, Natalka, Wiesiu and Julas. Thank you for always putting up with me, listening to my concerns and providing me with mental support.

Abstract

The purpose of this work is the further development of the lifting line code, by taking first steps towards the application of the wake expansion effect in the wind turbine design procedure. First, the theory and its practical implementation in the lifting line model is discussed. The approach to the wake expansion, the relevant theory, and the necessary assumptions are presented along the way.

The main goal of the conducted analysis is to explore effects of the newly introduced wake expansion on the results of the existing lifting line model with the use of the wake alignment procedure. The results are compared to the ones obtained without the application of the wake expansion and discussed in the light of the results and conclusions of previous contributors to the lifting line code.

Convergence studies were performed, and converged solutions could be successfully obtained. However, when the wake alignment procedure is applied, the model is still sensitive to numerical disturbances and the input parameters should be chosen carefully. Interestingly, the introduction of the wake expansion in some cases improves the results' stability both in the overall behavior of the wake geometry and in the local variables distributions. This further translate into more reliable values of the power coefficient predicted by the wind turbine load design optimization with the lifting line model.

From the conclusions, the reasons behind the encountered problems are discussed and the possible ways for future work on the lifting line code development are presented.

Keywords: Wind Turbines; Lifting Line Theory; Wake Alignment; Wake Expansion; Optimization.

Resumo

O objetivo deste trabalho foi o desenvolvimento de um código de linha sustentadora com a introdução do efeito de expansão de esteira no projeto aerodinâmico de turbinas eólicas. Primeiramente, descreve-se a teoria e a implementação prática do modelo de linha sustentadora. Em seguida, apresenta-se a abordagem à expansão da esteira, incluindo a teoria e os pressupostos necessários.

O principal objetivo foi explorar os efeitos da expansão de esteira nos resultados do procedimento de otimização do projeto com o modelo de linha sustentadora. Os resultados foram comparados aos obtidos sem a aplicação da expansão de esteira e discutidos à luz dos resultados de trabalhos anteriores, realizados no âmbito do desenvolvimento do código de linha sustentadora.

Ao longo do trabalho realizaram-se estudos de convergência, obtendo-se soluções convergentes. No entanto, quando o procedimento de alinhamento de esteira foi aplicado, o modelo ainda apresentou alguma sensibilidade a perturbações numéricas, sendo necessário que os parâmetros de entrada sejam escolhidos de forma cuidadosa. Em alguns casos verificou-se que a introdução da expansão de esteira melhorou a estabilidade dos resultados, tanto no comportamento geral da geometria de esteira, como nas distribuições das variáveis locais. Estes resultados traduzem-se em valores com maior grau de confiança do coeficiente de potência previsto pela otimização do projeto de carga da turbina eólica com o modelo da linha de sustentadora.

Nas conclusões foram discutidas as razões que desencadearam os problemas encontrados, assim como os trabalhos futuros que poderão ser executados no desenvolvimento de um código de linha sustentadora.

Palavras-chave: Turbinas eólicas; Teoria da linha sustentadora; Alinhamento de esteira; Expansão de esteira; Otimização.

Contents

List of Tables

List of Figures

Nomenclature

Greek symbols

α	Angle of attack
β	Undisturbed aerodynamic pitch angle
β_i	Induced aerodynamic pitch angle
Γ	Circulation
γ	Intensity of the trailing vortices
ε	Drag-to-lift ratio
ε_N	Numerical tolerance for the aerodynamic pitch angle
ε_W	Angular position of the kth lifting line
κ_N	Under-relaxation factor for the aerodynamic pitch angle
κ_W	Under-relaxation factor for the wake dimensionless pitch and tangential velocity
λ	Tip speed ratio
ν	Kinematic viscosity of the fluid
ξ	Coefficient of the empirical Hoshino function
ρ	Volumetric mass density of the fluid
ψ	Blade pitch angle
ω	Angular velocity of the rotor

Roman symbols

a	Axial induction factor
c	Section chord
C_1, C_2	Auxiliary coefficients used to account for the hub radius in the expansion procedure
C_D	Drag coefficient
C_L	Lift coefficient

C_P	Power coefficient
C_T	Axial force coefficient
C_{T_0}	Imposed axial force coefficient
$C_{a,t_{ij}}$	Axial and tangential influence coefficients matrices
CS	Control surface
CV	Control volume
D	Drag force per unit span
$\vec{e}$	Unit vector
$f(\xi)$	Empirical Hoshino function
H	Auxiliary function used in the Lagrange Multiplier Method
l	Constant; Lagrange multiplier
$\vec{L}$	Lift force by unit span
L_k	Lifting line *k*
M	Number of segments in which the lifting line is discretized
N	Number of sections in which a trailing vortex is discretized
n_s	Number of wake alignment sections
N_t	Number of equal stream-wise segments per revolution used in the wake discretization
p	Dimensionless wake pitch
Q	Torque
$\vec{R}$	Vector which goes from the integration point to the point where the induced velocity is being computed
R	Rotor radius
r_h	Hub radius
$\bar{r}_i$	Radial position of control point *i*
r_j	Radial position of end point *j*
r_{max}	Dimensionless maximum radius of the expansion
R_{max}	Maximum radius of the expansion
s	Stream-wise direction
S_k	Vortex sheet shed from lifting line *k*

T	Axial force
U	Velocity of the incoming flow
$\vec{V}$	Total velocity
$\vec{V}_\infty$	Undisturbed velocity
$\vec{v}$	Velocity induced by the entire system of vortices
V	Magnitude of projection of the total velocity vector on the blade cross section
$\vec{v}_k$	Velocity induced by the k^{th} lifting line and its sheet of trailing vortices
x, r, θ	Cylindrical coordinates in the rotating reference frame
x_0	Axial position at which the expansion starts
x_{fw}	Axial position of the far wake section
x_{ult}	Axial position of the end of the expansion zone
x_{uw}	Axial position of the ultimate section, where the wake is truncated
Z	Number of rotor blades

Subscripts

a	Projection on the axial direction
r	Projection on the radial direction
t	Projection on the tangential direction
x	Projection on the direction of *x*
y	Projection on the direction of *y*
z	Projection on the direction of *z*

Superscripts

$'$	Relative to the image vortex
$*$	Non-dimensional quantity

1 Introduction

1.1 State of the art

The end of the 19th century is considered to be a breakthrough period for the advancements in the aerodynamics and fluid mechanics field. It is at that time when the Chief Engineer and General Manager of The Lanchester Motor Company, Frederick W. Lanchester, after thoroughly studying the flight characteristics, established the basics of the lifting line theory [1]. Basing his reasoning on the previously published Helmholtz's theorems [2], which proved that a vortex could not simply vanish at the tip of the wing, Lanchester suggested [3] that this vortex would shed from the tip of the wing and continue in the wake.

In 1918, Ludwig Prandtl [4] along with his students, Albert Betz and Max Munk presented a more rigorous and accurate approach, according to which, vortex loses intensity along the whole wingspan because it is shed as a vortex-sheet from the trailing edge, not just at the wing-tips .

These bases of the lifting theory gave rise to many important and groundbreaking innovations in the fields of lifting surfaces such as propellers, wings and horizontal axis wind turbines.

In fact, lifting line theory was applied to propellers by Betz in 1919 [5]. Known as 'Classical Optimization", his solutions optimized the propellers, but were based on several limiting assumptions, such as having a light load and absence of viscous forces. The potential flow problem posed by Betz was only later resolved by Goldstein [6] in 1929 by considering a hubless propeller.

In 1952, Lerbs [7] managed to expand the range of the lifting theory application to also include moderately loaded propellers. Basing his thinking on the induction factor concept elaborated by Kawada [8] he figured out analytical expressions for the computation of the velocities induced by the system of vortices.

Maekawa [9] adapted the theories of Betz and Goldstein in order to present the design procedure of the wind turbines.

The theory was later developed even further by authors such as Kerwin [10], who focused on the aerodynamic design problem, and Coney [11], who tackled the issue of geometrical design.

The incorporation of viscous drag by Adkins & Liebeck [12] applied in 1994 was one of the most important corrections to the theory. This, as well as a vortex lattice model to discretize the wake was later used by Chattot [13] in the design of the wind turbines in 2003. The latter allowed him to compute the induced velocities with the use of numerical integration of the Biot-Savart law.

The introduction of the discretization made it possible to apply the wake alignment schemes. That allowed the modelling of the wakes with variable geometry by aligning it with the local velocities at multiple axial stations – the examples of that can be found in the works of Kinnas [14], Aran [15], and Diniz [16].

Throughout the years, there have been many contributions to address the problem of optimization. In example, the introduction of a variational approach – an alternative to the classical optimization, by authors such as Yim [17] and Kerwin [10] or a more modern contributor Epps, who with the use of his open source software OpenProp [18] [19] explored new wake models [20] and a lifting line/momentum-theory hybrid approach [21].

Much credit is also due to the research group led by Falcao de Campos and Baltazar that has been actively contributing to the lifting line theory. A lifting line code developed by them was implemented by Duarte [22] [23] in 1997 and is still being improved up to this date. Machado [24] [25] in 2010 used the effect of the hub in a design routine for marine turbines. In 2014 Caldeira [26] simulated the effects of drag by implementing a source model. Last, but not least, Melo [27] [28] in 2016 continued Caldeira's analysis of wind turbines and included a wake alignment scheme and Sousa [29] made the optimization procedure adjusting the analysis code by Melo and implementing the Lagrange multiplier method.

1.2 Objectives

The objective of this thesis is the further development of the lifting line code, created at IST by authors mentioned in the previous section, by implementation of the wake expansion in the wind turbine design procedure. The baseline for this work is the algorithm coded in *FORTRAN*, recently enriched in the wake alignment procedure by Melo and Lagrange multiplier optimization method by Sousa, under the supervision of Baltazar.

So far the effect of the wake expansion was neglected in this research and the wake was considered to be perfectly cylindrical. However, as the wake expansion is an obvious consequence of the exertion of the kinetic energy from the wind inflow (this will be discussed in Section 2.4), the introduction of the wake expansion may hypothetically contribute to more realistic results of the lifting line model.

As we are in an exploratory phase the necessary assumptions upon the parameters of the wake expansion needed to be made. Those apply to the geometry of the transition zone in which the expansion occurs, namely the length of this zone and the slope of the wake control surface.

After complementing the model with the wake expansion, the goal is to conduct the convergence analysis and parametric studies, and to examine its influence on the wake alignment procedure results. Along all those analyses, the performance of the turbine design with and without considering the effect of the wake expansion will be compared.

1.3 Thesis outline

The thesis is divided into the following chapters:

- The Chapter 2 presents the theoretical foundations of the lifting line theory for the wind turbines. Here, step by step, all the crucial definitions, physical phenomena and dependencies are explained, to arrive at the system of vortices that models the wind turbine rotor and the wake. This is the part where the approaches to the wake expansion are introduced and discussed.
- In Chapter 3 we focus on the implementation of the theory to make it useful for practical application. We discuss the numerical model and all its aspects that need to be taken into account, namely discretization of the system of vortices including newly implemented wake expansion procedure, calculating the induced velocities, modelling the rotor hub and methods of the optimization. Finally, the consecutive steps of the computational procedure including the wake alignment scheme are presented and explained in detail.
- In Chapter 4 the results of all tests mentioned in Section 1.2 are presented. Those include the convergence analysis, i.e. the sensitivity of the model to the discretization and numerical procedure parameters as well as some parametric studies. Moreover, the influence of the wake alignment stations configuration on the wake geometry, solution stability and expected turbine performance was examined. Where applicable, tests also include the comparison between case with and without the application of the wake expansion.
- Finally, in Chapter 5 we summarize the conclusions and suggestions for further development of the lifting line model in terms of the wake expansion procedure.

2 Theory

2.1 Introduction to the lifting line theory

The English engineer, Frederick W. Lanchester (1868 – 1946), was the first one who connected lift with the circulation [1]. He attempted to publish his ideas, however, his work was not broadly adopted by the scientific community at the time.

Completely independently, without knowledge about Lanchester's point of view, German mathematician, M. Wilhelm Kutta (1867 – 1944) came up with a concept that there must be a connection between lift force and circulation. However, in his work from 1902 he didn't formulate the precise dependency. The one that for the first time in history derived a quantitative relation between lift and circulation was Russian scientist, Nikolai Y. Joukowski (Zhukouski) (1847 – 1921). In his paper from 1906 he suggested the formula:

$$\vec{L} = -\rho \vec{V}_\infty \times \vec{\Gamma}, \tag{2.1}$$

where $\vec{L}$ is the lift force by unit span, ρ is the volumetric mass density of the fluid, $\vec{V}_\infty$ is the velocity of the undisturbed flow and $\vec{\Gamma}$ is the velocity circulation. The equation is known as the "Kutta-Joukowski theorem" and it states that on an infinite body of constant cross-section the lift force per unit span is proportional to the velocity circulation around this body.

One could assume, that to analyze a finite, three-dimensional wing it could be enough to slice the wing into multiple cross-sections called airfoils and to consider lift of each two-dimensional slice individually. However, adding up contributions of all slices gives grossly imprecise results, thus real three-dimensional wing cannot be simply modelled as series of two-dimensional, independent cross-sections which have no influence on one another. In reality forces acting on each airfoil are considerably affected by neighboring wing segments.

The person who developed the first practical theory that predicts lift of a finite wing was German physicist, Ludwig Prandtl (1875-1953). It is still in use nowadays for initial calculations of three-dimensional finite wings characteristics based on its geometry. The lifting line theory takes into account the interactions between wing sections and thus eliminates some of the errors in the two-dimensional approach.

The flow of the fluid around the airfoil translates into a difference in pressure between lower and upper surface of the wing. In the case of the three-dimensional finite wing, this differential will gradually decrease towards the tip, where eventually will become zero. As lift force is proportional to mentioned pressure difference and Kutta-Joukowski theorem relates lift with the circulation around the wing, the

spanwise change in pressure difference is equivalent to the spanwise change in the circulation which according to Helmholtz theorem, must result in shedding a sheet of free vortices downstream to the flow.

The theory of the abovementioned system of vortices created behind the wing applies also to analysis of the aerodynamic performance of wind turbine blades and will be further discussed in this chapter.

2.2 System of vortices

Consider the rotor of a horizontal wind turbine rotating with constant angular velocity $\vec{\omega}$ in a uniform inflow field with velocity $\vec{U}$ aligned with the axis of rotation. The rotor has radius R and Z blades symmetrically distributed around the hub of radius r_h. We define a Cartesian coordinate system (x, y, z) and a cylindrical reference frame rotating with the turbine rotor (x, r, θ) in which a relative velocity field is $\vec{U}_\infty = \vec{U} - \vec{\omega} \times \vec{r}$ as depicted in Figure 2.1.

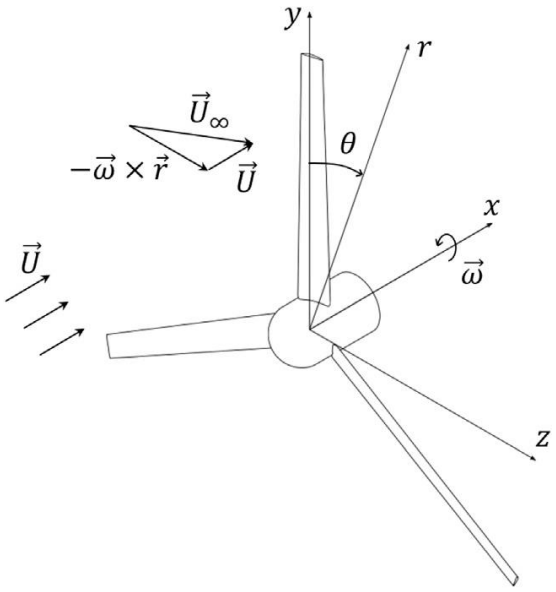

Figure 2.1: Considered coordinate systems and uniform inflow velocity fields (from [27])

Now, let us recall that in the lifting line theory, the lifting body is modelled as a bound vortex called a lifting line. As stated in the previous section, lift force is proportional to circulation which in the potential flow can be represented by a vortex extending from the root to the tip, with coordinates:

$$r_h < r < R, \qquad \theta_k = \frac{2\pi(k-1)}{Z}, \qquad k = 1, \dots, Z. \tag{2.2}$$

This vortex is characterized by the spanwise variation of the circulation given by:

$$\vec{\Gamma}(r) = -\Gamma\,(r)\vec{e}_r, \tag{2.3}$$

where $\vec{e}_r$ is a radial unit vector. As circulation goes to zero at the blade tip and according to Helmholtz theorem vortex cannot begin or terminate in a fluid, the variation of the circulation causes shedding of sheet of trailing vortices from the lifting line downstream to the flow shown in Figure 2.2. The intensity of this semi-infinite vortex sheet is proportional to this variation of circulation and expressed by:

$$\vec{\gamma} = \frac{d\Gamma\,(r)}{dr}\vec{e}_s, \tag{2.4}$$

where $\vec{e}_s$ is a unit vector tangent to the vortex sheet and aligned with the vortex filaments.

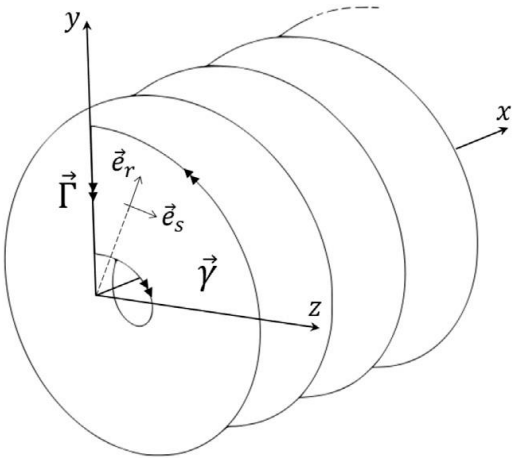

Figure 2.2: System of vortices for a single lifting line (from [27])

In the force-free vortex wake the vortex filaments must be aligned with the local velocity field, so that:

$$\vec{\gamma} \times \vec{V} = 0. \tag{2.5}$$

Without considering the influence of the vortices, the velocity field in the rotating reference frame is:

$$\vec{V}_\infty(x, r, \theta) = (U, 0, \omega r) \tag{2.6}$$

To account for the influence of system of vortices introduced into a uniform flow we will use Biot-Savart law, according to which the velocity induced by *k*th lifting line can be calculated at any point in the field by:

$$\overrightarrow{v_k}(x, y, z) = \frac{1}{4\pi}\int_{L_k} \frac{\vec{\Gamma} \times \vec{R}}{\left|\vec{R}\right|^3} dl + \frac{1}{4\pi}\int_{S_k} \frac{\vec{\gamma} \times \vec{R}}{\left|\vec{R}\right|^3} dS, \tag{2.7}$$

where $\vec{R}$ is the position vector that goes from the integration point to the considered field point (x, y, z) with module $\left|\vec{R}\right|$. The integration is performed along the lifting line L_k and the surface of the sheet of trailing vortices shed from this line along the wake, S_k. It is important to remark that when we compute velocities induced only at the lifting lines we can omit first integral – due to the symmetry of the rotor

influences of the lifting lines cancel each other out and only the trailing vortices have to be taken into account:

$$\overrightarrow{v_k}(x,y,z) = \frac{1}{4\pi}\int_{Sk} \frac{\vec{\gamma}\times\vec{R}}{\left|\vec{R}\right|^3} dS. \tag{2.8}$$

The total induced velocity is a sum of contributions of all Z blades, i.e. Z lifting lines and their corresponding vortex sheets:

$$\vec{v}(x,y,z) = \sum_{k=1}^{Z} \overrightarrow{v_k}(x,y,z). \tag{2.9}$$

Having that established, the total velocity field is a sum of undisturbed flow $\vec{U}_\infty$ (Equation 2.6) and velocity induced by system of vortices $\vec{V}$, so that in the cylindrical coordinates:

$$\vec{V}(x,r,\theta) = (U - v_a,\ v_r, \omega r + v_t), \tag{2.10}$$

where v_a, v_r and v_t denote respectively the axial, radial and tangential components of induced velocity and are expressed by:

$$v_a = -v_x, \tag{2.11a}$$

$$v_r = v_y cos\theta + v_z sin\theta, \tag{2.11b}$$

$$v_t = -v_y sin\theta + v_z cos\theta, \tag{2.11c}$$

where θ is the angular coordinate in the $y{-}z$ plane of coordinate system.

2.3 Forces, angles and coefficients

To discuss forces resulting from interaction between fluid and blades let's recall Kutta-Joukowski theorem (Equation 2.1):

$$\vec{L} = -\rho\vec{V}\times\vec{\Gamma}. \tag{2.12}$$

This formula gives lift force per unit span, which, by definition, is perpendicular to the incoming flow. Moreover, as both circulation vector $\vec{\Gamma}$ and radial component of the induced velocity $\vec{v}_r$ are aligned with the lifting line, the cross product $\vec{v}_r \times \vec{\Gamma}$ will be equal to zero. In means that radial components (i.e. parallel to the lifting line) of the induced velocities do not contribute to the lifting force. Following that, the magnitude of the lift force per unit span is expressed by:

$$L = \rho V \Gamma. \tag{2.13}$$

At each radial position along lifting lines the flow can be assumed as approximately two-dimensional as shown in Figure 2.3.

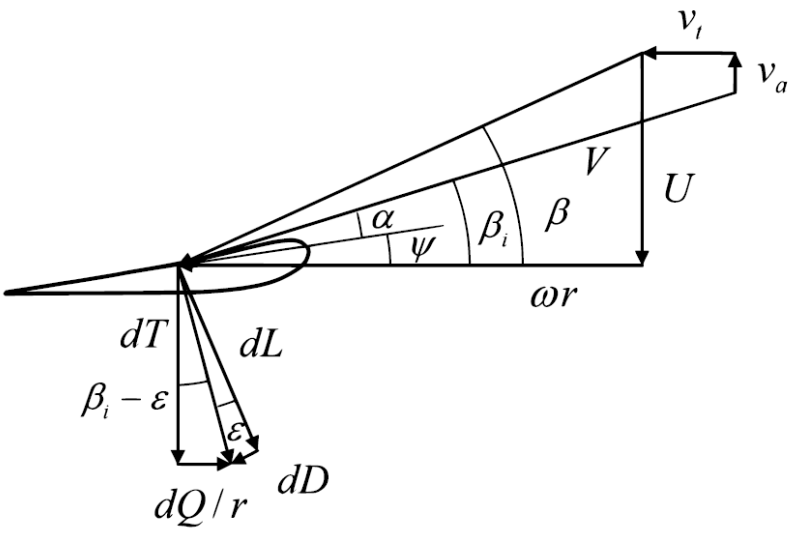

Figure 2.3: Velocity and force triangles at a blade section (from [31])

The total velocity experienced by the blade that includes influence of induced velocities is given by:

$$V = \sqrt{(U - v_a)^2 + (\omega r + v_t)^2} \tag{2.14}$$

Before further analysis of forces, let's identify some angles and forces from Figure 2.3. In the velocity triangle:

- β – the undisturbed aerodynamic pitch angle, which is the angle between the undisturbed velocity and the tangential direction, defined by:

$$tan\,\beta = \frac{U}{\omega r} = \frac{1}{\lambda r^*}, \tag{2.15}$$

  where $r^* = r/R$ is the dimensionless radius and λ is the tip speed ratio:

$$\lambda = \frac{\omega R}{U}. \tag{2.16}$$

- β_i – the induced aerodynamic pitch angle, which includes the effect of the axial and tangential induced velocities:

$$tan\,\beta_i = \frac{U - v_a}{\omega r + v_t} = \frac{1 - v_a^*}{\lambda r^* + v_t^*}, \tag{2.17}$$

  where $v_{a,t}^* = v_{a,t}/U$ represents dimensionless induced velocities.

- α – the angle of attack, which is the angle between the section chord line and the velocity projected on the blade cross section.
- ψ – blade pitch angle, which is the geometrical angle between the blade chord line and the tangential direction, given by:

$$\psi = \beta_i - \alpha. \tag{2.18}$$

The components of the forces triangle are:

- *L* – lift per unit span, is the component of the resulting force perpendicular to the inflow velocity vector $\vec{V}$,
- *D* – drag per unit span, the consequence of the viscous effects, which is the component of the resulting force parallel to the direction of the inflow velocity vector $\vec{V}$,
- *T* – thrust, axial force aligned with the axis of rotation,
- *Q/r* – circumferential force, which contributes to the torque, acting the tangential direction.

We introduce the dimensionless lift, drag, axial force and power coefficients, expressed respectively by:

$$C_L = \frac{L}{\frac{1}{2}\rho V^2 c} = \frac{2\Gamma}{Vc} = \frac{2\Gamma^*}{V^* c^*}, \tag{2.19}$$

$$C_D = \frac{D}{\frac{1}{2}\rho V^2 c}, \tag{2.20}$$

$$C_T = \frac{T}{\frac{1}{2}\rho U^2 \pi R^2}, \tag{2.21}$$

$$C_P = \frac{P}{\frac{1}{2}\rho U^3 \pi R^2} = \frac{\omega Q}{\frac{1}{2}\rho U^3 \pi R^2}. \tag{2.22}$$

The star * above the symbol denotes, that the value is dimensionless, thus $\Gamma^* = \Gamma/(UR)$, $c^* = c/R$ and V^* is the dimensionless form of the Equation 2.14:

$$V^* = V/U = \sqrt{(1 - v_a^*)^2 + (\lambda r^* + v_t^*)^2}. \tag{2.23}$$

The C_L and C_D are defined in an analogous way and are the function of the angle of attack α and the Reynolds number $Re = Vc/\nu$, where ν is the kinematic viscosity of the fluid. Their values are characteristic for a given airfoil and are obtained experimentally or by applying numerical methods. At this point, it is worth to mention an important parameter describing the role of viscous effects, i.e. drag to lift ratio defined by:

$$\varepsilon = D/L = C_D/C_L. \tag{2.24}$$

Remembering that L is lift force per unit span, for the axial force T we can write equation that will relate this force to the circulation Γ, analogous to Equation 2.13:

$$\frac{dT}{dr} = \rho(\omega r + v_t)\Gamma(r). \tag{2.25}$$

Now, we have to integrate this formula for axial force per unit span along all Z blades and to account for viscous effects we introduce ε. In such way we obtained the expression for total axial force:

$$T = \rho Z \int_{r_h}^{R} (\omega r + v_t) \Gamma(r)(1 + \varepsilon \tan \beta_i)\, dr, \tag{2.26}$$

which substituted to Equation 2.21 and considered in non-dimensional variables gives:

$$C_T = \frac{2Z}{\pi} \int_{r_h^*}^{1} (\lambda r^* + v_t^*) \Gamma^* (1 + \varepsilon \tan \beta_i)\, dr^*. \tag{2.27}$$

Following the same steps for the power coefficient we finally get:

$$C_P = \frac{2Z\lambda}{\pi} \int_{r_h^*}^{1} (1 - v_a^*) \Gamma^* \left(1 - \frac{\varepsilon}{\tan \beta_i}\right) r^* dr^*. \tag{2.28}$$

2.4 Modeling of wake expansion

The wind turbine converts kinetic energy of the inflowing fluid into rotational energy of the turbine's rotor. As part of the fluid energy is extracted by the rotor, velocity of the fluid downstream the rotor must decrease compared to the inflow velocity. As the flow is assumed to be incompressible and mass flow must be conserved, slowing down the fluid results in the expansion of the wake.

In order to analyze the effect of the wake expansion we need to point out the following aspects:

- axial position of the end of the expansion zone – the region in which wake is expanding,
- radius of the fully expanded wake,
- function defining the shape of the expanded wake.

Starting with the axial position of the end of the expansion zone x_{ult}, from the theoretical point of view, it should be assigned to the axial station at which the radial component of the induced velocity becomes negligible. However, because of the difficulties related to the practical application of this approach, in the used computational code x_{ult} is not related with any other variable, i.e. it can be arbitrarily imposed as an input parameter. As the variations of the intensity of trailing vortices are more pronounced near the rotor and their influence on the lifting line decrease with the increasing distance it is reasonable to consider lengths of the expansion zone not longer than a few rotor radii e.g. from $x/R = 1$ to $x/R = 5$. Moreover, it seems convenient to couple the end of the expansion zone with the last alignment station, which makes it to coincide with the end of the transition wake and the beginning of the far wake. The details of the transition wake will be analyzed more carefully in Section 3.1.

To define the radius of the fully expanded wake, we will use the actuator disc theory. Figure 2.4. shows an actuator disc, which is a theoretical representation of the wind turbine rotor, extracting energy from the uniform inflow with velocity U. Extraction of the kinetic energy slows down the fluid and, together with the mass flow conservation, causes expansion of the stream-tube.

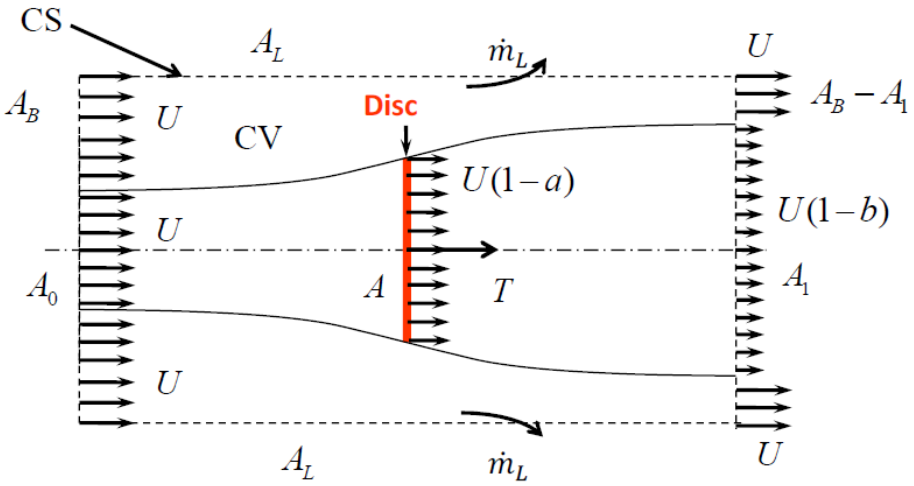

Figure 2.4: The actuator disc extracting energy from the fluid and the stream-tube (from [32])

The axial force acting uniformly on a disc is:

$$T = 2\rho A U^2 a(1-a), \tag{2.29}$$

where a is the axial flow induction factor. Equation 2.29 substituted to Equation 2.21 gives:

$$C_T = 4a(1-a) \Rightarrow a = \frac{1}{2}\left(1 - \sqrt{1 - C_T}\right). \tag{2.30}$$

Mass flow rate inside the stream-tube is:

$$\dot{m} = \rho A_{disc} V_{disc} = \rho A_1 V_1 \Rightarrow \frac{A_{disc}}{A_1} = \frac{V_1}{V_{disc}}, \tag{2.31}$$

where A_{disc}, A_1, V_{disc} and V_1 are surface areas and fluid velocities at the actuator disc and far downstream (i.e. at the boundary of the control volume CV) respectively, given by: $A_{disc} = \pi R^2$, $V_{disc} = U(1-a)$, $A_1 = \pi R_{max}^2$, $V_1 = U(1-2a)$, where R is the radius of the actuator disc (turbine rotor) and R_{max} is the radius of the fully expanded wake. Combining all we obtain the formula for the dimensionless radius of the fully expanded wake:

$${r_{max}}^* = \frac{R_{max}}{R} = \sqrt{\frac{1}{2}\left(\sqrt{\frac{1}{1-C_T}} + 1\right)}, \tag{2.32}$$

which is dependent on the axial force coefficient C_T i.e. on the turbine load.

The non-dimensional radius of the expanded wake will change along the axial coordinate from 1 to ${r_{max}}^*$ according to the expression:

$${r_t}^*(x) = 1 + ({r_{max}}^* - 1) \cdot f\big(\xi(x)\big), \tag{2.33}$$

where $f(\xi)$ is a polynomial function. Subscript t indicates that Equation 2.33 applies to the blade tip.

In this thesis, the expression originally proposed by Hoshino [33] for the contraction of the propeller wakes will be adapted for the purpose of the wind turbine wake expansion. The formula, from this point on called occasionally the empirical function, is given by:

$$f(\xi) = \sqrt{\xi} + 1.013\xi - 1.920\xi^2 + 1.228\xi^3 - 0.321\xi^4, \tag{2.34}$$

with:

$$\xi(x) = \frac{x - x_0}{x_{ult} - x_0}, \tag{2.35}$$

where x is the axial coordinate at which the expanded radius is computed, and x_0 is the axial station at which the expansion starts. Since expansion starts at the rotor plane $x_0 = 0$ and:

$$\xi(x) = \frac{x}{x_{ult}}. \tag{2.36}$$

Note, that as x varies from 0 to x_{ult}, value of ξ changes linearly from 0 to 1. Therefore, as an alternative to the empirical function 2.34, linear expansion of the wake can be applied simply by replacing Equation 2.33 with:

$$r_t{}^*(x) = 1 + (r_{max}{}^* - 1) \cdot \xi(x). \tag{2.37}$$

Shapes of the two functions that can be used to expand the wake radius are depicted in Figure 2.5.

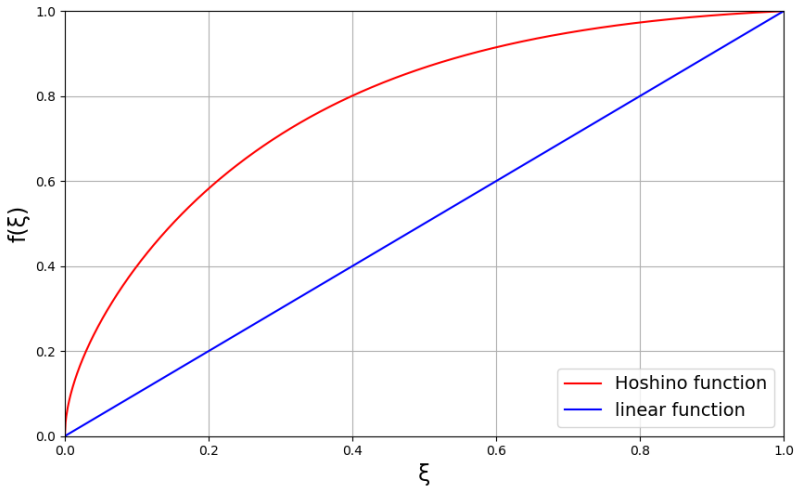

Figure 2.5: Functions used to define the shape of the expanded wake

3 Numerical model

In this chapter we will analyze how the theory presented in the Chapter 2. was implemented in a computational code. Since all the variables in following chapters will be non-dimensional, we will cease to use a star superscript *.

3.1 Discretization

Lifting line

Lifting line is a bound vortex of varying circulation along its length. As this continuous change cannot be numerically modeled, the lifting line must be discretized into M vortex segments characterized by constant circulation Γ_i. It means, that in the computational procedure the continuous variation of the lifting line intensity is represented in a stepwise manner. In this thesis points that bound vortex segments are called *end points* - r_j, and points placed in the center of the segments are called *control points* - $\bar{r}_i$, as shown in Figure 3.1.

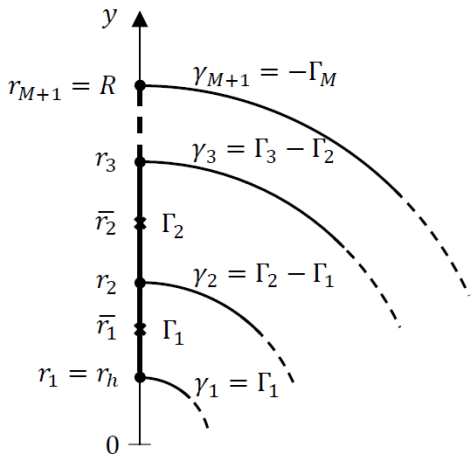

Figure 3.1: Discretization of the lifting line (from [27])

Let's remind that in the infinite blade of constant cross-section geometry the circulation is assumed to be constant and the variation of circulation appears in the case of the finite blade, as the circulation at the tip goes to zero. Hence, the gradient of circulation is expected to be larger near the blade tip and it is reasonable to apply a denser discretization in this region. Radial coordinates of the control and end points were computed according to the half-cosine distribution:

$$\bar{r}_i = r_h - (1 - r_h)\, cos\left(\frac{\pi/2(i - 1/2)}{M} + \frac{\pi}{2}\right), \qquad i = 1, \ldots, M \tag{3.1}$$

$$r_j = r_h - (1 - r_h)\, cos\left(\frac{\pi/2(j - 1)}{M} + \frac{\pi}{2}\right), \qquad j = 1, \ldots, M + 1 \tag{3.2}$$

Wake

In the simpler case without the wake expansion, the wake is assumed to be cylindrical. If we additionally assume constant pitch distribution along the axial direction, we obtain perfectly helicoidal wake vortices and the analytical approach can be applied to compute induced velocities (Morgan and Wrench (1966) computational formulas [34]). The code allows to align the wake at a number of axial stations, defined among the input parameters. In such case, the wake will be characterized by changing its geometry and we need to employ numerical integration in order to compute velocities induced by trailing vortices which are no longer helicoidal. Moreover, the purpose of this thesis is to examine the influence of the wake expansion which, by definition, assumes a change of the wake geometry and thus excludes considerations of helicoidal wake vortices and the analytical solution. Hence, similarly to the lifting line, the vortex sheet shed downstream to the wake which is theoretically continuous must be discretized into a finite number of concentrated vortices. The lifting line divided into M vortex segments sheds $M + 1$ trailing vortices. Those vortices start at the end points of the lifting line segments, as depicted in Figure 3.1, and have intensity equal to the drop of lifting line circulation at the specific points:

$$\gamma_1 = \Gamma_1, \qquad \gamma_j = \Gamma_j - \Gamma_{j-1}, j = 2, \ldots, M, \qquad \gamma_{M+1} = -\Gamma_M. \tag{3.3}$$

Each of the $M + 1$ trailing vortices is further discretized into a number of N segments which depends on two input parameters: N_t – the number of streamwise segments equally distributed per one revolution and x_{uw} – the axial coordinate of the ultimate section, where the wake is truncated, determining the axial length of the wake. In this way we obtain the mesh of the wake geometry, as in Figure 3.2, in which nodes are the end points of the trailing vortices segments.

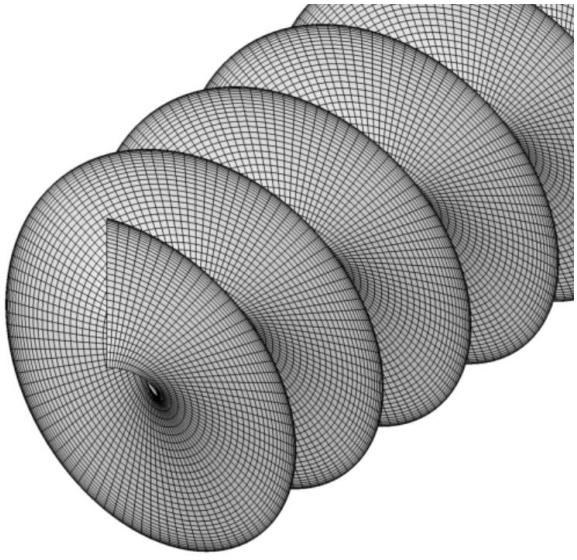

Figure 3.2: Discretized wake – one blade only

To better understand how input parameters shape the wake geometry, example from Figure 3.3 shows the discretized wake, truncated after one blade revolution, in which lifting line consists of $M = 10$ segments and sheds $M + 1 = 11$ trailing vortices, and one blade revolution is represented by $N_t = 20$ streamwise segments. Note that, according to half-cosine stretching function, discretization of the lifting line gets denser as we approach the blade tip.

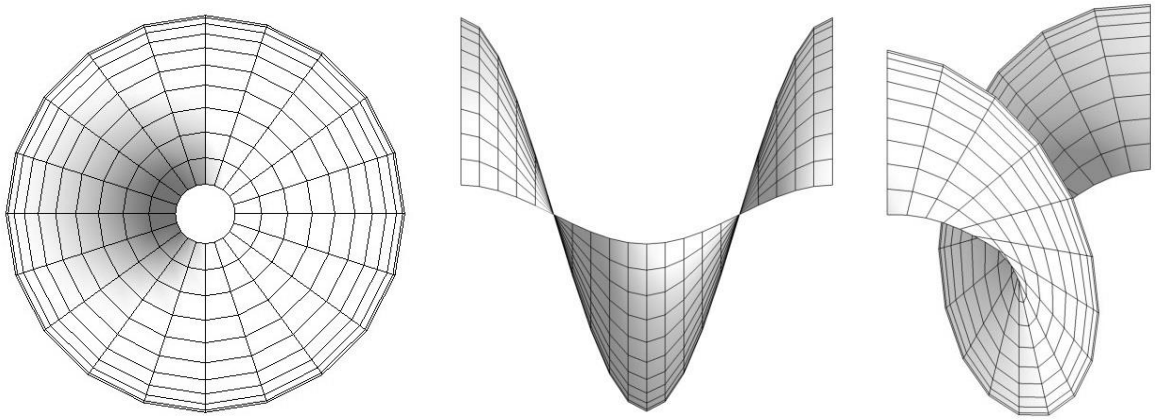

a) view aligned with rotation axis b) view perpendicular to rotation axis c) view from an angle

Figure 3.3: Example of the wake discretization for one revolution of one blade

To apply numerical integration, the wake geometry must be defined, i.e. cylindrical coordinates of all nodes in the wake mesh must be computed. When computations are done without the wake alignment, the wake geometry is computed only once (*the initial wake*). When the alignment scheme is used, the new wake geometry (*the new wake*) is computed in every iteration (the procedure will be described in Section 3.5) and we can distinguish two wake regions:

1. Transition wake – the zone between the lifting lines ($x = 0$) and the far wake station x_{fw} in which the geometry changes along the axial coordinate and the wake expands. In this region a set of n_s alignment sections is defined ($x_1, \dots, x_{n_s}$) and a far wake station is assigned to the last of them: $x_{fw} = x_{n_s}$. At each alignment section the induced velocities are computed for all $M + 1$ trailing vortices. To compute induced velocities between the alignment sections, linear interpolation along the axial direction is used. Next, the axial and angular coordinates of consecutive vortex segment's end points are computed recursively by:

$$x_{j,n+1} = x_{j,n} + p_{j,n}\left(1 + \frac{v_{t_{j,n}}}{\lambda r_j}\right)\frac{2}{N_t}, \tag{3.4}$$

$$\theta_{j,n+1} = x_{j,n} + \left(1 + \frac{v_{t_{j,n}}}{\lambda r_j}\right)\frac{2\pi}{N_t}, \tag{3.5}$$

   where p is non-dimensional wake pitch given by $p = \pi r \, tan \, \beta_i$.
2. Ultimate wake – the zone between the far wake station x_{fw} and the ultimate wake station x_{uw} at which the wake is truncated, as the influence of induced velocities further downstream

becomes negligible. In this region v_t and p remain constant and have values computed at x_{fw}. Here the wake is already fully expanded and trailing vortices are helicoidal lines.

Note, that to compute x coordinates, we need p which depends on r. To define *initial wake* for the purpose of the first iteration, while computing x coordinates, we assume the wake to be cylindrical: $r_{j,n+1} = r_{j,n}$. This assumption must be done, as radii computed using the expansion formulas discussed in Section 2.4 depend on the axial coordinate x. However, at the end of defining *initial wake* new radial coordinates are computed to account for the wake expansion. Similarly, coordinates of the expanded radial coordinates are updated at the end of every iteration when *new wake* is computed. The implementation of the expansion will be presented in the following paragraph.

Expanded radii

Each of n axial wake stations consist of j trailing vortices segments' end points. First, we need to compute radii of those points in the fully expanded wake. Next step will be applying the expansion function given by Equation 2.33, which will relate the amount of the expansion with the axial coordinate. Note, that we want to keep the hub radius constant along whole wake i.e. to keep modelling a cylindrical hub (modelling the hub will be discussed in Section 3.3). Hence, expansion in radial direction occurs only between the hub and the tip vortex. To prevent hub radius from stretching we use linear transformation and the radial coordinates of fully expanded trailing vortices end points are:

$$r_{max,j} = r_j \cdot C_1 + C_2, \tag{3.6}$$

where C_1 and C_2 are coefficients given by:

$$C_1 = \frac{r_{max} - r_h}{r - r_h}, \qquad C_2 = r_h(1 - C_1), \tag{3.7}$$

and r_{max} is the fully expanded radius of trailing vortex shed from the blade tip, i.e. maximum radius of the fully expanded wake.

Now, we can discuss how functions used to shape the wake expansion are applied in the computational procedure. As an example, we will focus on the expansion with the empirical function 2.34. The radial coordinate of the n^{th} segment end point of the j^{th} trailing vortex is defined by:

$$r_{j,n} = r_j + \left(r_{max,j} - r_j\right) \cdot f(\xi_n). \tag{3.8}$$

where $f(\xi)$ is a polynomial function:

$$f(\xi_n) = \sqrt{\xi_n} + 1.013\xi_n - 1.920{\xi_n}^2 + 1.228{\xi_n}^3 - 0.321{\xi_n}^4, \tag{3.9}$$

and ξ_n coefficient is:

$$\xi_n = \frac{x_n - x_0}{x_{fw} - x_0}, \tag{3.10}$$

where x_n is the axial coordinate of the n^{th} wake segment, x_{fw} is the far wake station (i.e. the axial coordinate of the end of the expansion zone). We can transform this equation similarly to Equation 2.35:

$$\xi_n = \frac{x_n}{x_{fw}}. \tag{3.11}$$

The presented method allows to expand the wake in the radial direction as shown in Figure 3.4.

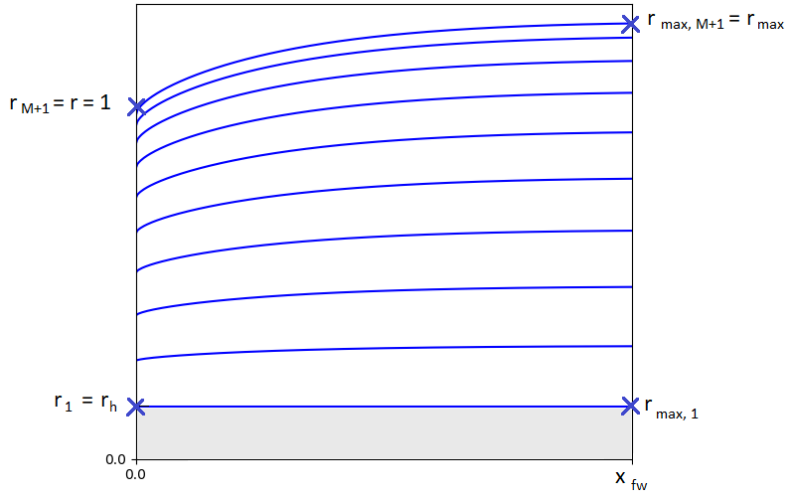

Figure 3.4: Expected radial expansion of the trailing vortices

Looking at Figure 3.4. we can notice that the first trailing vortex, i.e. the one shed from the lifting line at the hub radius, does not expand, and hence $r_1 = r_h = r_{max,1}$. Moreover, the further we move from the hub radius, the more pronounced is expansion of the trailing vortices.

3.2 Induced velocities

The induced velocities computational procedure is based on Biot-Savart law (Equation 2.7) transformed into form:

$$v_{a,t_i} = \sum_{j=1}^{M} C_{a,t_{ij}} \Gamma_j, \tag{3.12}$$

in which $C_{a,t_{ij}}$ are axial and tangential influence coefficient matrices. Those coefficients are function of the wake geometry. Depending on the needs, two methods can be used to compute the matrices:

1. Analytical approach – used when alignment scheme is not applied. In such case trailing vortices are perfectly helicoidal and the induced velocities need to be calculated only at the lifting line. Knowing the parameters that define the wake geometry, i.e. number of rotor blades – Z, distribution of control and end points – $\bar{r}_i$ and r_j, and the induced aerodynamic pitch angle – $tan\,\beta_i$, we can use Lerbs' analytical expressions (Morgan and Wrench [34], 1966).

2. Numerical approach – used when wake is aligned and thus its geometry varies along the axial direction. In this case, we apply the numerical integration implemented by Melo [28]. To do so, we discretize Equation 2.7 to obtain:

$$\vec{v}(x,y,z) =$$

$$= -\sum_{k=1}^{Z}\sum_{i=1}^{M}\frac{1}{4\pi}\left(\int_{r_{j_i}}^{r_{j_{i+1}}}\frac{\vec{e}_r^{\,k}\times\vec{R}}{\left|\vec{R}\right|^3}dr + \int_{L_{j_{i+1}}^k}\frac{\vec{e}_{t_{j_{i+1}}}^{\,k}\times\vec{R}}{\left|\vec{R}\right|^3}ds_{j_{i+1}}^k - \int_{L_{j_i}^k}\frac{\vec{e}_{t_{j_i}}^{\,k}\times\vec{R}}{\left|\vec{R}\right|^3}ds_{j_i}^k\right)\Gamma_i. \tag{3.13}$$

With this formula we can calculate the velocity induced by the system of vortices at any point. The first integral considers the influence of the i^{th} lifting line segment and is solved analytically, while the remaining two account the influence coming from trailing vortices shed from the end points of relevant lifting line segments (from r_{j_i} to $r_{j_{i+1}}$).

The analytical method works well in the simplified cases which do not require wake discretization – it is fast and does not bare high computational costs. The numerical approach allows to introduce the wake alignment and expansion, so it does not constraint the wake geometry. However, it is much more complex which results in a longer and more demanding computation of the solution.

3.3 Hub model

We consider finite span blades and thus each of one-dimensional lifting lines (i.e. straight-line bound vortices) representing them must have two boundaries that need to be included in the numerical model. One boundary is the blade tip, where circulation goes to zero, as it was discussed in Section 2.1. The other one is the rotor hub. In this case we cannot use the same approach as for the tip because the hub constitutes a physical barrier. A convenient solution proposed by Kerwin [35] is to model the hub as a solid cylinder of a radius r_h along the whole wake. To do so, we introduce a system of image vortices which consists of $M + 1$ image vortices, one for each of trailing vortices. Their intensities are symmetrical to the ones of trailing vortices:

$$\gamma_j{}' = -\gamma_j, \tag{3.14}$$

their radial coordinates are given by:

$$r_j{}' = \frac{{r_h}^2}{r_j}, \tag{3.15}$$

and their induced aerodynamic pitch angles are:

$$(tan\,\beta_i)_j{}' = (tan\,\beta_i)_j\frac{r_j}{r_j'}. \tag{3.16}$$

The radial component of the velocity induced by such pair of vortices cancels at all points on the surface of the hub modelled as a cylinder of radius r_h [35]. An example of trailing vortex and its corresponding image vortex is presented in Figure 3.5.

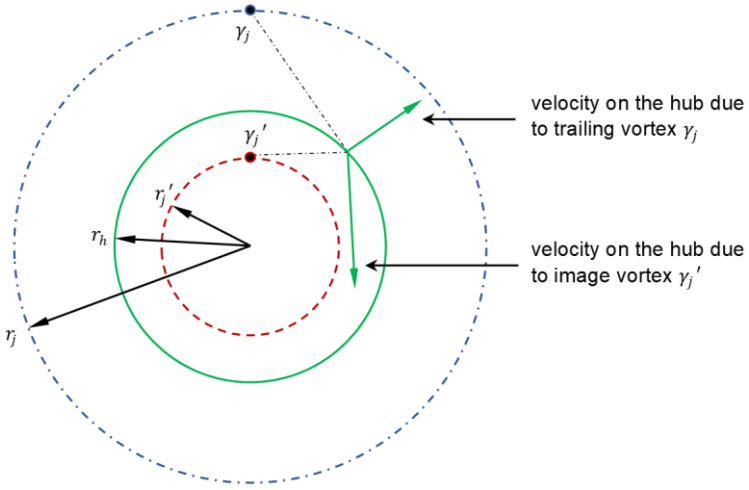

Figure 3.5: Two-dimensional illustration of the pair of vortices and corresponding induced velocities (from [35])

Finally, the hub effect is included in the numerical model by subtraction of image vortex system influence coefficients matrix from the original vortex system matrix:

$$C_{a,t_{ij}}{}^{total} = C_{a,t_{ij}} - C_{a,t}{}'_{ij}. \tag{3.17}$$

3.4 Optimization

Having discussed all aspects of the turbine rotor modelling, we can now focus on the crucial part of the computational procedure – the optimization. The goal is to optimize circulation distribution over the lifting line $\Gamma(r)$ to obtain maximum efficiency for the imposed load (thrust coefficient C_T) [21]. In the turbine design problem, it is equivalent to maximize torque represented by power coefficient C_P. Optimum circulation distribution together with chosen lift coefficient distribution $C_L(r)$ can be used to define blade design, i.e. chord and geometrical pitch distribution, by using Equations 2.19 and 2.18. The computational code allows to choose between two methods of the optimization which are described below.

Classical Optimization

As explained by Sousa [29], assuming uniform inflow and neglecting viscous forces, the loss of kinetic energy is minimized in the far wake when input to output power ratio is independent of the radial coordinate. If we also assume that $v_a \ll U$ and $v_t \ll \omega r$, which is right in case of light turbine loads, the

condition to meet in order to obtain the optimum circulation distribution, called 'Lerbs criterion', is given by:

$$\frac{(tan\,\beta_i)_i}{(tan\,\beta)_i} = constant, \qquad i = 1, \dots, M. \tag{3.18}$$

We will denote this constant as l. Remembering Equation 2.15 we can reformulate this criterion to:

$$\bar{r}_i (tan\,\beta_i)_i = l. \tag{3.19}$$

Substituting the induced aerodynamic pitch angle $tan\,\beta_i$ from Equation 2.17 and further induced velocities from Equation 3.12 we obtain:

$$\bar{r}_i \frac{1 - v_{ai}}{\lambda \bar{r}_i + v_{ti}} - l = \bar{r}_i - \bar{r}_i \sum_{j=1}^{M} C_{aij}\Gamma_j - l\lambda\bar{r}_i - l\sum_{j=1}^{M} C_{tij}\Gamma_j = \sum_{j=1}^{M}\left(C_{aij} + \frac{l}{\bar{r}_i}C_{tij}\right)\Gamma_j + l\lambda - 1. \tag{3.20}$$

In such way we formulated the system of equations used to calculate optimum circulation distribution:

$$\sum_{j=1}^{M}\left(C_{aij} + \frac{\hat{l}}{\bar{r}_i}C_{tij}\right)\Gamma_j + l\lambda = 1, \qquad i = 1, \dots, M. \tag{3.21}$$

Note, that l is still unknown, thus, it is convenient to use an estimation $\hat{l}$ where it multiplies with Γ_j, to linearize the system of equations. In every iteration $\hat{l}$ is replaced with the l obtained in the previous one. So far, our system consists of M equations and $M + 1$ unknowns. We will complement it with the discretized form of Equation 2.27:

$$C_{T_0} = \frac{2Z}{\pi}\sum_{i=1}^{M}\left\{\left(\lambda\bar{r}_i + v_{t_i}\right)(1 + \varepsilon_i(tan\,\beta_i)_i)\Delta r_i \Gamma_i\right\}, \tag{3.22}$$

where C_{T_0} is the load imposed on the turbine and Δr_i is the length of the i^{th} lifting line segment.

In addition, the optimization procedure uses Equation 3.21 and Equation 3.22 to find turbine load C_{T_0} for which power coefficient C_P is maximized. This will be further discussed in the next section.

Lagrange Multiplier Method

One more time we will follow steps described by Sousa [29]. In this method the auxiliary function is defined:

$$H = C_P + l\left(C_T + C_{T_0}\right), \tag{3.23}$$

and to find maximum power coefficient C_P for a given load C_{T_0} we must impose the conditions:

$$\frac{\partial H}{\partial \Gamma_i} = 0 \wedge \frac{\partial H}{\partial l} = 0, \qquad i = 1, \dots, M, \tag{3.24}$$

where l is the Lagrange multiplier.

To interpret the partial derivatives $\frac{\partial H}{\partial \Gamma_i}$ let's start with the discrete forms of Equation 2.27 and Equation 2.28:

$$C_T = \frac{2Z}{\pi}\sum_{i=1}^{M}\left\{\left(\lambda\bar{r}_i + v_{t_i}\right)\Gamma_i(1+\varepsilon_i(tan\,\beta_i)_i)\Delta r_i\right\}, \tag{3.25}$$

$$C_P = \frac{2Z\lambda}{\pi}\sum_{i=1}^{M}\left\{\left(1-v_{a_i}\right)\Gamma_i\left(1-\frac{\varepsilon_i}{(tan\,\beta_i)_i}\right)\bar{r}_i\Delta r_i\right\}. \tag{3.26}$$

Frist, we will focus on the part of the formula for the power coefficient responsible for inviscid contribution and we will use Equation 3.12 to make a substitution of induced velocities:

$$\frac{2Z\lambda}{\pi}\sum_{i=1}^{M}\left(1-v_{a_i}\right)\Gamma_i\bar{r}_i\Delta r_i = \frac{2Z\lambda}{\pi}\sum_{i=1}^{M}\left\{\Gamma_i\bar{r}_i\Delta r_i - \Gamma_i\bar{r}_i\Delta r_i\sum_{j=1}^{M}C_{a_{ij}}\Gamma_j\right\}. \tag{3.27}$$

Next, we will differentiate in Γ_i. Solution for the first term is easily obtained:

$$\frac{\partial}{\partial\Gamma_i}\left\{\frac{2Z\lambda}{\pi}\sum_{i=1}^{M}\Gamma_i\bar{r}_i\Delta r_i\right\} = \frac{\partial}{\partial\Gamma_i}\left\{\frac{2Z\lambda}{\pi}\left(\Gamma_1\bar{r}_1\Delta r_1 + \Gamma_2\bar{r}_2\Delta r_2 + \ldots + \Gamma_M\bar{r}_M\Delta r_M\right)\right\} = \frac{2Z\lambda}{\pi}\bar{r}_i\Delta r_i. \tag{3.28}$$

The second term costs a little more effort. At the beginning we will expand:

$$\begin{aligned}\sum_{i=1}^{M}\left\{\Gamma_i\bar{r}_i\Delta r_i\sum_{j=1}^{M}C_{a_{ij}}\Gamma_j\right\} &= \Gamma_1\bar{r}_1\Delta r_1\left(C_{a_{11}}\Gamma_1 + C_{a_{12}}\Gamma_2 + \ldots + C_{a_{1M}}\Gamma_M\right) + \\ &+ \Gamma_2\bar{r}_2\Delta r_2\left(C_{a_{21}}\Gamma_1 + C_{a_{22}}\Gamma_2 + \ldots + C_{a_{2M}}\Gamma_M\right) + \ldots \\ &= C_{a_{11}}\Gamma_1^{*2}\bar{r}_1\Delta r_1 + C_{a_{12}}\Gamma_1\Gamma_2\bar{r}_1\Delta r_1 + C_{a_{21}}\Gamma_2\Gamma_1\bar{r}_2\Delta r_2 + \ldots\end{aligned} \tag{3.29}$$

and, according to Kerwin [10], assume that $\frac{\partial C_{a,t_{ij}}}{\partial\Gamma_i} = 0$, then the differentiation in Γ_i yields:

$$\begin{aligned}&\frac{\partial}{\partial\Gamma_i}\left(C_{a_{11}}\Gamma_1^{*2}\bar{r}_1\Delta r_1 + C_{a_{12}}\Gamma_1\Gamma_2\bar{r}_1\Delta r_1 + C_{a_{21}}\Gamma_2\Gamma_1\bar{r}_2\Delta r_2 + \ldots\right) = \\ &= 2C_{a_{11}}\Gamma_1\bar{r}_1\Delta r_1 + C_{a_{12}}\Gamma_2\bar{r}_1\Delta r_1 + C_{a_{21}}\Gamma_2\bar{r}_2\Delta r_2 + \ldots \\ &= \sum_{j=1}^{M}\left(C_{a_{1j}}\Gamma_j\bar{r}_1\Delta r_1 + C_{a_{j1}}\Gamma_j\bar{r}_j\Delta r_j\right).\end{aligned} \tag{3.30}$$

Hence, we arrive at the expression:

$$\frac{\partial}{\partial \Gamma_i}\left(\sum_{i=1}^{M}\left\{\Gamma_i \bar{r}_i \Delta r_i \sum_{j=1}^{M} C_{a_{ij}}\Gamma_j\right\}\right) = \sum_{j=1}^{M}\left(C_{a_{ij}}\Gamma_j \bar{r}_i \Delta r_i + C_{a_{ji}}\Gamma_j \bar{r}_j \Delta r_j\right). \tag{3.31}$$

Following analogous steps for the remaining derivatives we obtain system of equations with total $M+1$ equations and $M+1$ unknowns:

$$\begin{aligned}
&\frac{\partial H}{\partial \Gamma_i} = 0 \Leftrightarrow \\
&\Leftrightarrow \sum_{j=1}^{M}\left\{\begin{bmatrix} -\lambda\left(1-\frac{\varepsilon_i}{(tan\,\beta_i)_i}\right)\left(C_{a_{ij}}\bar{r}_i\Delta r_i + C_{a_{ji}}\bar{r}_j\Delta r_j\right) + \\ +\hat{l}(1+\varepsilon_i(tan\,\beta_i)_i)\left(C_{t_{ij}}\Delta r_i + C_{t_{ji}}\Delta r_j\right)\end{bmatrix}\Gamma_j\right\} + \\
&+\{\lambda(1+\varepsilon_i(tan\,\beta_i)_i)\bar{r}_i\Delta r_i\}l = -\lambda\left(1-\frac{\varepsilon_i}{(tan\,\beta_i)_i}\right)\bar{r}_i\Delta r_i, \qquad i=1,\dots,M,
\end{aligned} \tag{3.32}$$

$$\frac{\partial H}{\partial l} = 0 \Leftrightarrow C_{T_0} = \frac{2Z}{\pi}\sum_{i=1}^{M}\left\{\left(\lambda\bar{r}_i + v_{t_i}\right)(1+\varepsilon_i(tan\,\beta_i)_i)\Delta r_i \Gamma_i\right\}. \tag{3.33}$$

As in the classical optimization, to linearize the system of equations we use an estimation $\hat{l}$ where necessary and the final goal of the optimization procedure is to find turbine load C_{T_0} for which power coefficient C_P is maximized, by satisfying Equation 3.32 and Equation 3.33.

3.5 Computational procedure

In this section we will analyze the computational procedure of the aerodynamic design problem algorithm coded in *FORTRAN* language. As already mentioned in Section 3.1, the wake expansion requires the use of a numerical method, thus we will focus on the algorithm including wake alignment procedure shown in Figure 3.6. Note, that the code still allows to run calculations without the wake alignment and expansion, by using a simplified version of the algorithm presented below.

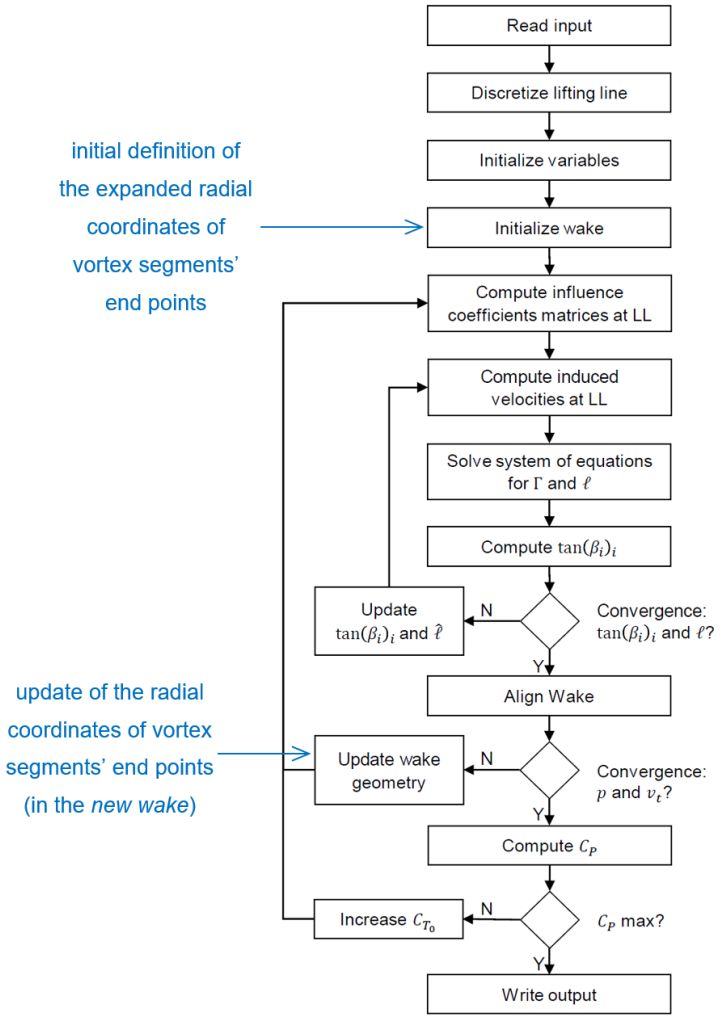

Figure 3.6: Flowchart of the computational procedure (from [29])

The wake expansion formulas discussed in Section 3.1are implemented in two places of the algorithm. First, in the *initial wake* definition and then in the *new wake* definition, after the alignment procedure, as shown in Figure 3.6. The reason for that will be explained further in this section.

Now, we will analyze the algorithm in detail and explain the consecutive stages. The computational procedure always starts with a few initial steps, namely:

- reading the input, which is the set of parameters imported from the text file, including parameters regarding both the aerodynamic design (e.g. number of blades or tip speed ratio) and numerical issues (e.g. discretization details, tolerances or under-relaxation factors),
- discretizing lifting line, discussed in Section 3.1,
- initializing yet unspecified variables, by setting their values to zero, except from the undisturbed aerodynamic pitch angle, which at this stage is not influenced by the induced velocities $v_{a,t} = 0$, and takes the value:

$$tan\,\beta_i = tan\,\beta = \frac{1}{\lambda r}, \tag{3.34}$$

- initializing the wake geometry, by computing axial and angular coordinates of vortex segments' and points using Equation 3.4 and Equation 3.5 and expanded radial coordinates using the procedure and equations described in Section 3.1,
- computing initial axial and tangential influence coefficients matrices $C_{a,t_{ij}}$, as described in Section 3.2,

Note that while initializing the wake geometry tangential induced velocity is equal to zero $v_{t_j} = 0$, we use the undisturbed aerodynamic pitch angle from Equation 3.34. Moreover, as in the case of wake expansion the Equation 3.4 for the axial and Equation 3.8 for the radial coordinates depend on each other, we first assume the cylindrical wake, next compute axial and angular coordinates, and at the end calculate expanded radii using axial coordinates. This simplifies the computational procedure.

Next, we enter the most inner loop, in which we iteratively compute $tan\,\beta_i$ until we achieve a desired precision, i.e. we meet the convergence criterion within the set tolerance. In this cycle the steps are:

- computing induced velocities using Equation 3.12,
- solving the system of equations, to find new $\Gamma(r)$ and l, using one of the two optimization methods discussed in Section 3.4,
- updating the aerodynamic pitch angle $tan\,\beta_i$ with Equation 2.17,
- checking, whether the convergence criteria are satisfied, by comparing current values of $tan\,\beta_i$ and l with values obtained in previous iteration:

$$\left|\frac{(tan\,\beta_i)_i{}^{new} - (tan\,\beta_i)_i{}^{previous}}{(tan\,\beta_i)_i{}^{new}}\right| < \varepsilon_N \wedge \left|\frac{l^{new} - l^{previous}}{l^{new}}\right| < \varepsilon_N, \tag{3.35}$$

  where ε_N is a tolerance specified in the input.

The cycle is repeated until the convergence criteria are met, i.e. increment of $tan\,\beta_i$ and l in consecutive iterations becomes negligible. To increase numerical stability, we introduce under-relaxation with expression reducing impact of the new value of $tan\,\beta_i$ before starting the next iteration:

$$(tan\,\beta_i)_i{}^{next} = \kappa_N (tan\,\beta_i)_i{}^{new} + (1 - \kappa_N)(tan\,\beta_i)_i{}^{previous}, \tag{3.36}$$

where κ_N is under-relaxation factor defined among the input parameters.

Once the solution has converged and we have the circulation distribution at the lifting line $\Gamma(r)$ optimized for the given wake geometry, we move on to the wake alignment procedure. The number of the alignment sections and their axial coordinates are defined in the input file. The wake (i.e. lifting lines and trailing vortices) is already discretized (in the first iteration we use *initial wake*). Wake alignment is also done iteratively. The cycle for the wake alignment includes the already described inner cycle. After convergence in the inner loop is achieved, the next steps are:

- computing influence coefficients matrices at every point of alignment (i.e. intersection of the trailing vortices with the alignment plane at the axial coordinate of the alignment section),

- computing induced velocities and pitch at alignment points,
- checking, whether the convergence criteria are satisfied, by comparing current values of $tan\,\beta_i$ and l with values obtained in previous iteration:

$$\left|\frac{{p_j}^{new} - {p_j}^{previous}}{{p_j}^{new}}\right| < \varepsilon_W \wedge \left|\frac{{v_t}_j{}^{new} - {v_t}_j{}^{previous}}{{v_t}_j{}^{new}}\right| < \varepsilon_W, \tag{3.37}$$

  where ε_W is another tolerance specified in the input.

Note, that while computing induced velocities at alignment stations we take into account the influence of the lifting line (bound vortex), unlike in the calculations of induced velocities at the lifting line where it cancels out due to symmetry considerations (as already mentioned in Section 2.2).

If the convergence is not achieved yet, analogously to the inner loop, we use the under-relaxation factor κ_N set in the input and apply under-relaxation with equations:

$${p_j}^{next} = \kappa_N {p_j}^{new} + (1 - \kappa_N){p_j}^{previous}, \tag{3.38}$$

$${v_t}_j{}^{next} = \kappa_N {v_t}_j{}^{new} + (1 - \kappa_N){v_t}_j{}^{previous}. \tag{3.39}$$

Then, we update the wake geometry, so that the wake is aligned with the local velocities at the alignment points. The velocity and pitch between the alignment stations are computed using linear interpolation. Next, the axial and angular coordinates of the *new wake* are computed with Equation 3.4 and Equation 3.5. It is important to mention, that the axial length of the wake is defined as an input parameter x_{uw}/R and remains constant for the whole procedure. Hence, by changing the pitch in consecutive iterations we change the total number of the axial wake stations N. To prevent the expansion zone from stretching in an axial direction, at the end of each iteration on the wake alignment, we update radial coordinates of all the wake points. In this way, we keep the lengths of the expansion zone constant and equal to the length of the transition zone or, in other words, we always achieve fully expanded wake at the last alignment station. The *new wake* is then used in the next iteration and the cycle is repeated until the convergence criteria are satisfied.

After the successful wake alignment, we compute the power coefficient C_P using the solution obtained for the imposed load C_{T_0}. Next, we slightly increase the value of C_{T_0} and follow the whole computational procedure again from the beginning, creating the outer cycle from Figure 3.6. Repeating this multiple times gives us the curve which is $C_P(C_{T_0})$ characteristic, which according to Sousa [29], always has a maximum, which is an optimum point.

It is worth mentioning that the *FORTRAN* code allows to run calculations without the application of the wake alignment and expansion. In such simplified case we can use the analytical approach for the computation of the influence coefficient matrices, as already discussed in Section 3.2, and skip the loop on the wake alignment (we use only simplifies *initial* wake geometry and assume helicoidal trailing vortices filaments). This procedure is described step-by-step in Sousa [29].

4 Results

4.1 Convergence analysis

The numerical methods suffer from iterative error, round-off error and discretization error. In this section we will examine the influence of the latter one on the results. To do so, we will check the effect of changing input parameters responsible for the discretization of the wake. Similar analysis was done by Sousa [29], however, without the consideration of the wake expansion. As in this thesis we focus on the wake alignment and expansion, all tests require the use of the numerical approach. Therefore, the choice of the right values of input parameters is very important for obtaining convergent solutions and minimize the discretization error.

Prior to the tests, we define the input configuration considered to be typical for a design problem.

Number of Blades – Z	3
Hub Radius – r_h/R	0.15
Tip Speed Ratio – λ	7
Drag-to-Lift Ratio – ε	0.01
Number of lifting line segments – M	30
Interpolation	Linear
Integration	Numerical
Optimization	Lagrange
Imposed Load – C_{T_0}	0.8
Hub Correction	Yes
Point Distribution over the Lifting Line	Half-Cosine
Axial end wake station – x_{uw}/R	25
Number of Segments in One Revolution – N_t	100
Tolerance	10^{-3}

Table 4.1: Input parameters for the convergence analysis

Parameters listed in Table 4.1 (if not stated otherwise) are common for all test in the convergence analysis. Base values of some of them (e.g. M, x_{uw}/R and N_t) are adapted from Sousa [29], as indicated in his analysis to give the best results. All tests were performed using both expansion methods, and most of them repeated for one and three alignment stations. Some of them were additionally compared

with the case without the wake expansion. The detailed description of all tests can be found subsequent sections.

4.1.1 Lifting line discretization

In this section, the influence of the number of lifting line segments M on the computational model was examined. Tests were repeated for the linear expansion and for the empirical expansion function 2.34. The lifting line was discretized into 10, 20, 25, 30, 35, 40, 50 and 60 segments. Moreover, two wake alignment cases were considered:

- one alignment station at $x/R = \{0\}$ (alignment only at the lifting line) and length of the transition wake $x_{ult}/R = 2$ (Figure 4.1a),
- three alignment stations $x/R = \{0, 1, 2\}$, length of the transition wake $x_{ult}/R = 2$ (end of the expansion zone coinciding with the last alignment station) (Figure 4.1b).

We evaluate the convergence by analyzing how the number of lifting line segments influences the power coefficient C_P, as according to Sousa [29], it can be considered as a good overall convergence indicator. The results of the analysis are presented in Figure 4.1.

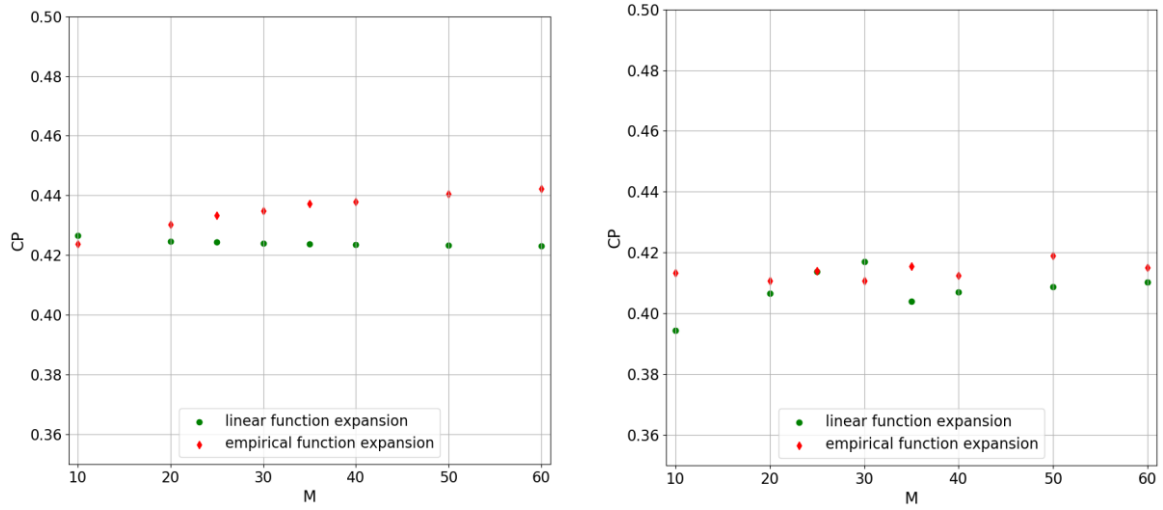

(a) one alignment station $x/R = \{0\}$ (b) three alignment stations $x/R = \{0, 1, 2\}$

Figure 4.1: The power coefficient for increasing number of the lifting line segments

When we focus on Figure 4.1a (one alignment station), we see that in case of linear expansion the influence of the number of the lifting line segments on the power coefficient is negligible, whilst in the case of the empirical function 2.34 we can notice that C_P is slightly increasing with the increase of M. However, since this value does not converge but gradually increases, we can interpret this as a numerical issue, not the real influence of the number of the lifting line segments. It is important to mention, that the slope of the empirical function 2.34 is very steep near the lifting line (as depicted in Figure 2.5 where the lifting line is theoretically at $\xi = 0$) and thus it was more difficult to obtain convergent solutions when this method was used.

In Figure 4.1b we can see that in case of three alignment stations the points are more scattered, however the variation of the power coefficient is not significant, especially in case of the empirical function 2.34 where the differences are in order of 10^{-3}. Here again, like in the case of one alignment station, the power coefficient does not seem to converge to a certain value, which indicates that we are dealing with numerical uncertainties, not the influence of the tested parameter.

Since the increase of the number of lifting line segments does not improve the convergence of the solution when we consider numerical integration with the wake expansion, the practical conclusion that can be drawn from this analysis is to keep $M = 30$, as indicated by Sousa.

Moreover, when comparing Figure 4.1a and Figure 4.1b we can notice, that values of the power coefficient in the case of three wake alignment stations are lower than in the case of wake aligned only at the lifting line (this will be also mentioned in Section 4.2.1).

4.1.2 Wake discretization

In this section we tested how wake discretization influences the overall convergence of the solution. The tests were run with different values of two parameters:

- the number of streamwise segments per one revolution $N_t = \{10, 100, 500, 1000\}$,
- the axial end wake station $x_{uw}/R = \{10, 25, 50\}$.

Tests were performed using the linear expansion method, the wake aligned at the lifting line and all combinations of the aforementioned discretization parameters. The results are presented in Figure 4.2.

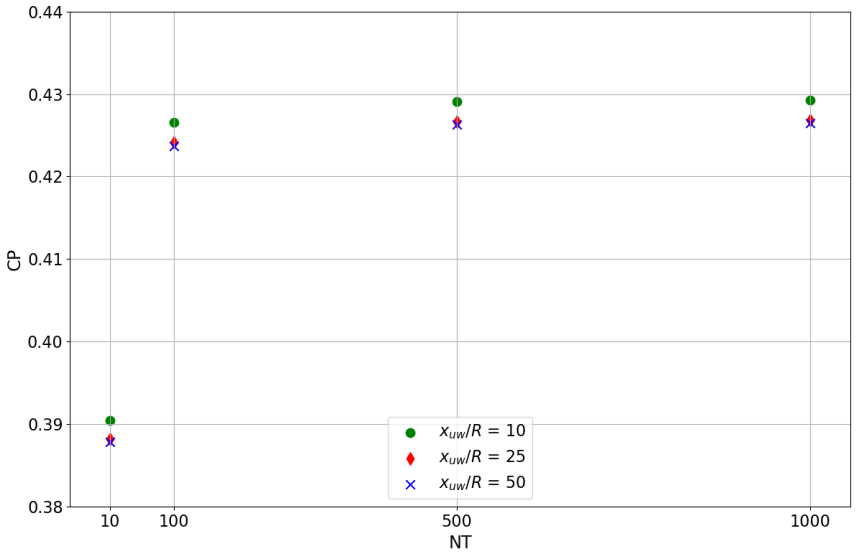

Figure 4.2: Convergence of the power coefficient with increasing number of stream-wise sections per one revolution N_t and axial wake length x_{uw}/R using linear wake expansion

Analyzing Figure 4.1 we can see, that the increase of number of stream-wise sections per one revolution from $N_t = 10$ to $N_t = 100$ results in the significant increase of the value of the power coefficient. The further increase of N_t does not bring a noticeable change of $C_P$value, which seem to eventually converge to around 0.43. As higher number of stream-wise sections per one revolution would contribute to the drastic increase of the computational cost, we decide to keep $N_t = 100$ for all the remining test in this thesis.

When we focus on the second parameter – the axial wake length x_{uw}/R, we can notice that the value of the power coefficient slightly decreases with its increase. It is worth to mention, that the difference of the power coefficient value becomes negligible when we move from $x_{uw}/R = 25$ to $x_{uw}/R = 50$. Once again, to avoid the additional computational cost we advise to use the axial wake length equal to $x_{uw}/R = 25$.

Similar analysis, yet without the effect of the wake expansion was done by Sousa [29]. He also proved that $N_t = 100$ and $x_{uw}/R = 25$ give satisfactory results in terms of the solution convergence. Hence, we can draw the conclusion, that introducing the wake expansion does not require the change of the discretization parameters compared to ones already indicated as the best for the case without the wake expansion.

Note that the tests were run only for the linear wake expansion, because higher values of stream-wise sections per one revolution N_t (i.e. $N_t = 500$ and $N_t = 1000$) in the case of the empirical function 2.34 resulted in problems with convergence and the data obtained from successful tests was not sufficient to be presented. However, the recommended values of $N_t = 100$ and $x_{uw}/R = 25$ proved to give convergent solutions in the case of empirical function expansion method.

4.2 Transition wake parameters

In this section we tested the influence of the parameters responsible for the shape of the transition zone on the results. Those are the parameters defining the wake alignment and expansion, i.e. the number and position of the wake alignment stations, length of the expansion zone (which is coincident with the last wake alignment station) and the radius of the fully expanded wake.

4.2.1 Number and position of the alignment stations

In calculations with the wake alignment procedure we need to make an important decision on the choice of the number and the axial position of the wake alignment stations. The parameter that have a substantial influence on the wake geometry is the position of the last alignment station, as it defines the

end of the transition wake and the expansion zone (after that axial point the wake parameters, such as radial position of the trailing vortices' segments or pitch distribution, remain constant).

In the first part of this analysis the wake was aligned at two stations and the length of the transition zone was being changed from $x_{ult}/R = 0.5$ up to $x_{ult}/R = 3$. Next, the intermediate aligned station was introduced at $x/R = 0.5 \cdot x_{ult}/R$, i.e. in the middle of the transition wake. Tests were repeated for three cases: without the wake expansion, with the linear expansion, and with the expansion using the empirical function 2.34. It is important to mention, that all tests were run using input parameters from Table 4.1 and the imposed load $C_{T_0} = 0.8$, which, according to Equation 2.32 results in the radius of the fully expanded wake equal to $r_{max}/R = 1.272$.

The performance of the individual cases was assessed against two criteria: the value of the power coefficient and the shape of the wake geometry. First, let's focus on C_P which values for different configurations of the wake alignment stations are presented in Table 4.2. Note that in some cases the calculations did not converge (e.g. empirical expansion and wake aligned at $x/R = \{0, 0.5\}$).

x/R	C_P		
	no expansion	linear expansion	empirical funtion expansion
$\{0, 0.5\}$	0.4610	0.4557	-
$\{0, 1\}$	0.4641	0.4473	0.4563
$\{0, 1.5\}$	0.4165	0.4476	0.4577
$\{0, 2\}$	0.4665	0.4494	0.4554
$\{0, 2.5\}$	0.4815	0.4578	0.4577
$\{0, 3\}$	0.4903	0.4628	0.4602
$\{0, 0.25, 0.5\}$	-	0.4453	-
$\{0, 0.5, 1\}$	0.4292	0.4424	0.4592
$\{0, 0.75, 1.5\}$	0.3795	0.4403	0.4473
$\{0, 1, 2\}$	0.3828	0.4462	0.4463
$\{0, 1.25, 2.5\}$	0.4385	0.4467	0.4474
$\{0, 1.5, 3\}$	0.4417	0.4567	0.4485

Table 4.2: Power coefficient for different configurations of the wake alignment stations

In the runs without the wake expansion the values of the power coefficient show large variation, from 0.3828 up to 0.4903. The introduction of the wake expansion reduces the variation, so that the results take values from 0.4403 to 0.4628 for linear expansion and from 0.4463 to 0.4602 for the empirical expansion function 2.34. The latter one yields in most cases slightly higher values of the power coefficient. Moreover, when the wake expansion procedure is applied, the introduction of the intermediate alignment station contributes to a minor decrease of the power coefficient.

The most important conclusion that can be drawn from Table 4.2 is that the length of the transition wake does not have a strong influence on the value of the power coefficient. Hence, to identify good configurations of the wake alignment stations we need to have a closer look at the wake geometries.

First, we need to establish, that we expect smooth wake geometries. Any sharp edges or fluctuations in the wake may indicate numerical problems in the iterative procedure. It is important to remind that the procedure responsible for the computation of the expanded radii does not take into account induced radial velocities, thus, according to Melo [27] and Sousa [29], a decrease of pitch near the blade tip is an expected effect, as it may be interpreted as a manifestation of the wake roll-up effect which is not modeled. The three-dimensional wake geometries of all cases listed in Table 4.2 can be found in appendices A. – C. Let's have a look at chosen wake geometries, that will help to draw meaningful conclusions. We will now analyze cases with three alignment stations, as they should reflect more details of the transition wake in which we expect rapid changes of the wake parameters and the wake shape. In Figure 4.3 we present the wake geometries of the chosen wake alignment stations configurations for the case without the wake expansion. Note, that to keep the figure clear, the wake of only one blade is plotted.

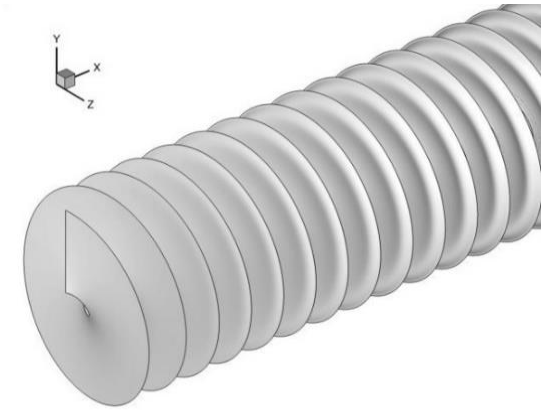

(a) $x/R = \{0, 0.5, 1\}$.

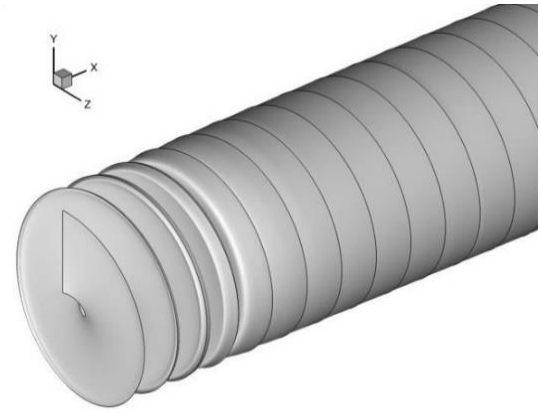

(b) $x/R = \{0, 0.75, 1.5\}$.

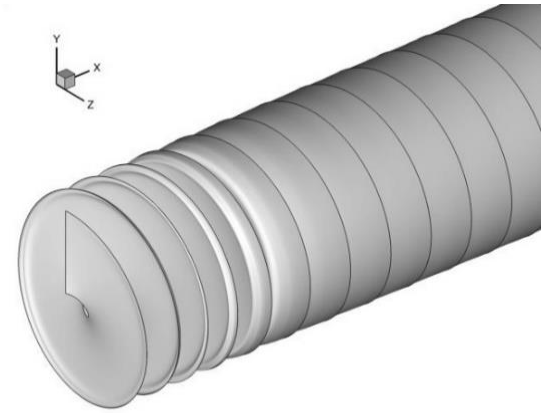

(c) $x/R = \{0, 1, 2\}$.

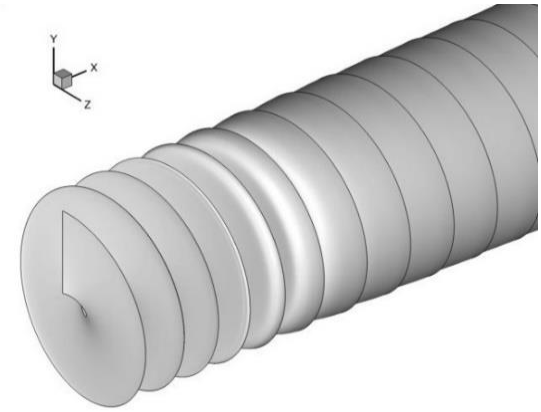

(d) $x/R = \{0, 1.25, 2.5\}$.

Figure 4.3: Chosen geometries of the wakes aligned at three stations – no expansion case

It is easy to notice, that for the length of the wake equal to $x_{ult}/R = 1$ (Figure 4.3a) the geometry is smooth, however, the effect of folding in the downstream direction at the blade tip is not strongly pronounced. When we move the last alignment station further in the axial direction (Figure 4.3b and 4.3c) we can notice oscillations in the wake pitch distribution – at some radial positions wake folds in the upstream direction – which is not a satisfactory result. However, in the last picture (Figure 4.3d) the wake have overall smooth and correct shape, thus $x/R = \{0, 1.25, 2.5\}$ will be the wake alignment stations configuration used in further tests without the wake expansion.

Moving on to the expanded wakes, let's start with linear expansion method. Chosen geometries are presented in Figure 4.4.

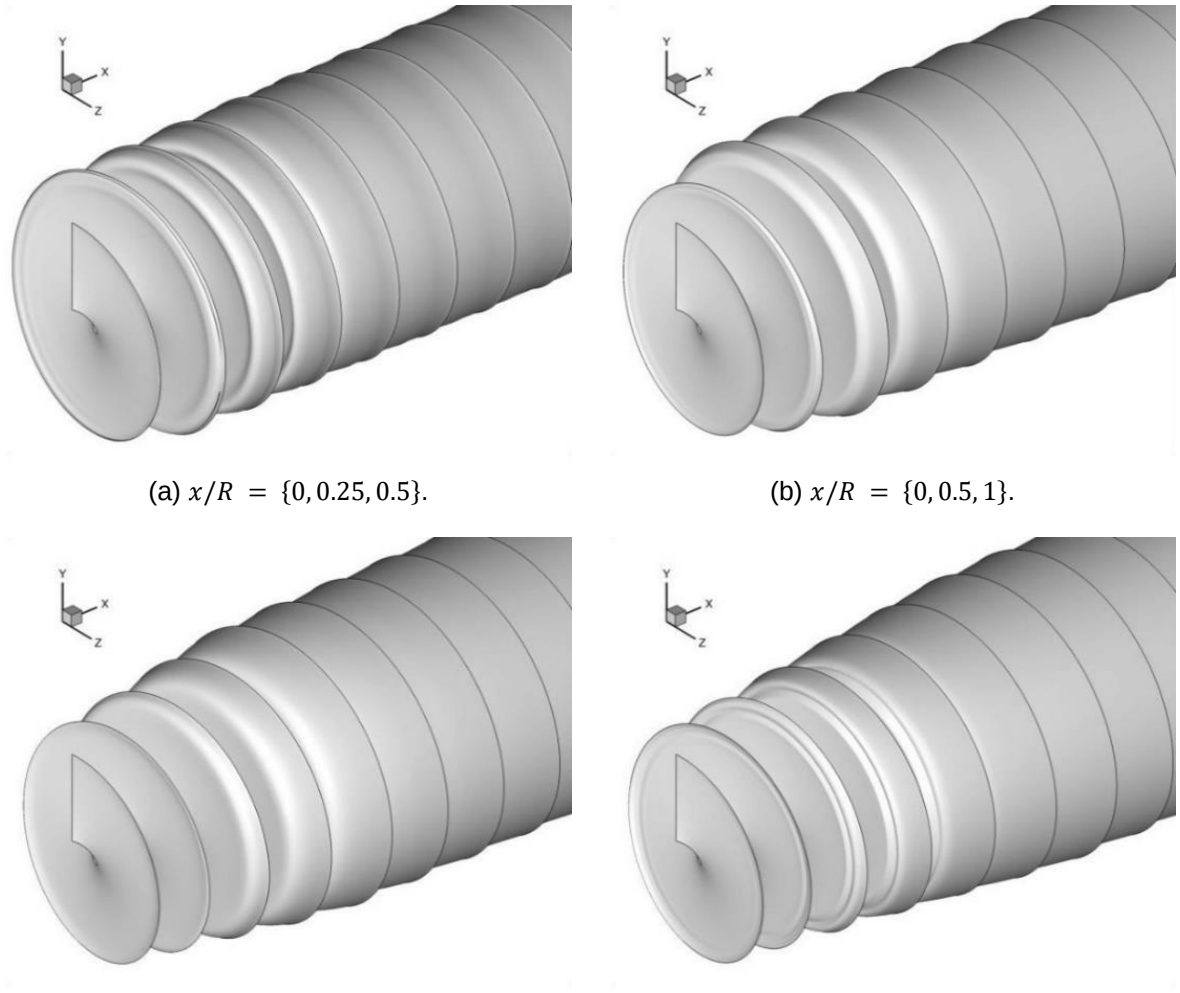

(a) $x/R = \{0, 0.25, 0.5\}$. (b) $x/R = \{0, 0.5, 1\}$.

(c) $x/R = \{0, 1, 2\}$ (d) $x/R = \{0, 1.5, 3\}$.

Figure 4.4: Chosen geometries of the wakes aligned at three stations – linear expansion case

When looking at the Figure 4.4 we can point out the wake aligned at $x/R = \{0, 1.5, 3\}$ (Figure 4.4d) as the one with the most oscillations. Furthermore, in case of short transition zones the expansion of the wake happens over very short axial distance (only 0.5 of the turbine radius in case of Figure 4.4a) which does not seem realistic. Figure 4.4c shows smooth wake geometry without any unexpected behavior, thus in case of linear expansion, for used set of input parameters, it is recommended to align the wake at $x/R = \{0, 1, 2\}$.

Next, we will analyze wakes expanded with the method using empirical function 2.34. Analogously to the previous cases, chosen wake geometries are depicted in Figure 4.5.

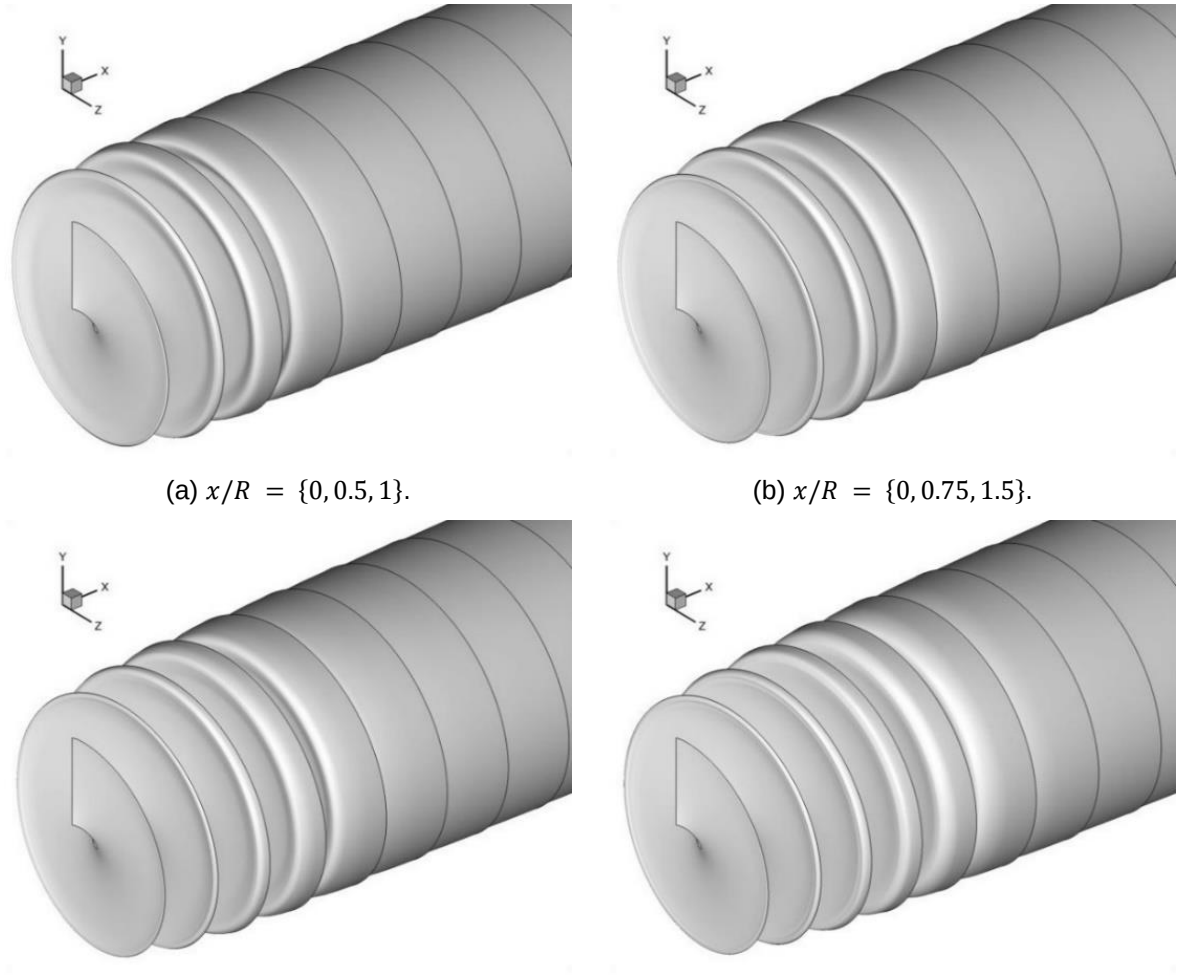

(a) $x/R = \{0, 0.5, 1\}$. (b) $x/R = \{0, 0.75, 1.5\}$.

(c) $x/R = \{0, 1, 2\}$. (d) $x/R = \{0, 1.5, 3\}$

Figure 4.5: Chosen geometries of the wakes aligned at three stations – empirical expansion case

In case of empirical function 2.34 expansion method, we can notice that as we approach the blade tip, the wake first fold in the upstream, and then (at the tip) in the downstream direction. This behavior is more pronounced in the case of shorter transition zones (Figure 4.5a and 4.5b). Similarly, to the linear expansion method, we recommend aligning the wake at $x/R = \{0, 1, 2\}$ as for this configuration its geometry have a correct overall baheviour.

Having decided upon the length of the transition zone equal to $x_{ult}/R = 2$ (last alignment station), which for both expansion methods seem to yield correct results, we will now check whether the position of the intermediate alignment station have a significant influence on the results. Note, that so far in all cases the intermediate alignment station was placed exactly in the middle of the transition wake.

For the purpose of this analysis, for each expansion method we performed four tests with different positions of the intermediate alignment stations. The values of the power coefficients are presented in Table 4.3.

x/R	C_P	
	linear expansion	empirical funtion expansion
$\{0, 0.25, 2\}$	0.4386	0.4547
$\{0, 0.5, 2\}$	0.4496	0.4615
$\{0, 0.75, 2\}$	0.4519	0.4387
$\{0, 1, 2\}$	0.4462	0.4463

Table 4.3: Power coefficient for different position of the intermediate alignment station

As it is hard to evaluate the performance of the particular configurations based only on the values of the power coefficient, once again we will have a look at the wake geometries which are plotted in the appendices B. and C. (see Figure B.3 and Figure C.3). To avoid unnecessary description of the geometries of all configurations we can draw a brief conclusion that position of the intermediate wake alignment station at $x/R = 1$ gives satisfactory, smooth wake geometries.

Moreover, the values of the power coefficient for wakes aligned at $x/R = \{0, 1, 2\}$ are very similar (see Table 4.3), what indicates that this configuration of the wake alignment stations will be a good foundation for further comparison of both expansion methods.

Finally, as we have chosen the "practical optimum" of the wake alignment stations configurations, let's have a look at the radial distributions of the pitch at the alignment stations which are plotted in Figure 4.6 for all the expansion cases (i.e. both expansion methods and case without the wake expansion). Note, that we use the recommended configurations of the alignment stations, i.e. $x/R = \{0, 1.25, 2.5\}$ in the case without the wake expansion and $x/R = \{0, 1, 2\}$ in the cases with the wake expansion.

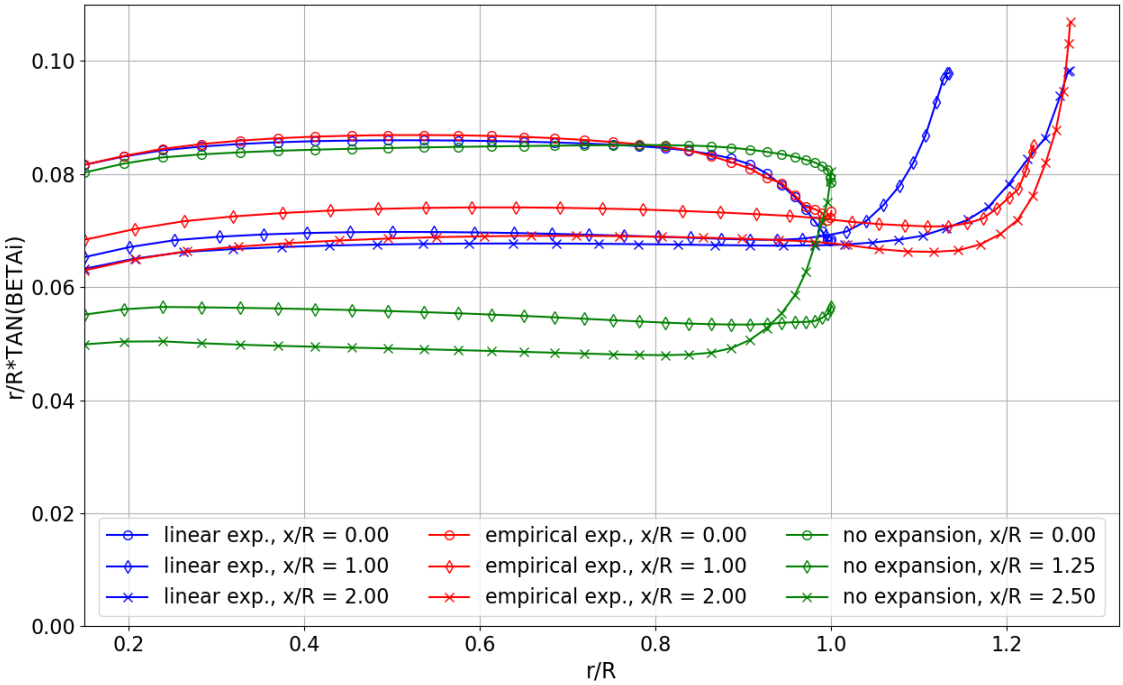

Figure 4.6: Radial pitch distribution at the alignment stations – all three expansion cases

In Figure 4.6 we can clearly see, that in all three cases, at the last alignment station the pitch increases as we approach the tip – this is what translates into the folding of the wake in the downstream direction. It is also easy to notice, that the pitch at second and third alignment station is much higher when the wake expansion procedure is applied. Moreover, when looking at the lines representing pitch distributions at the intermediate station ($x/R = 1$) we see, that in the case of the empirical function 2.34 expansion the wake is already almost fully expanded, even though it is just the middle of the transition zone. The reason for that is the very steep slope of the empirical function 2.34 (see Figure 2.5).

Now, let's focus on the distributions of the local variables over the lifting line. We will analyze values of the circulation, induced axial and tangential velocities, and induced aerodynamic pitch. In Figure 4.7 we can see the comparison of the three expansion methods for the wake aligned at the same configurations of the alignment stations as analyzed in the Figure 4.6.

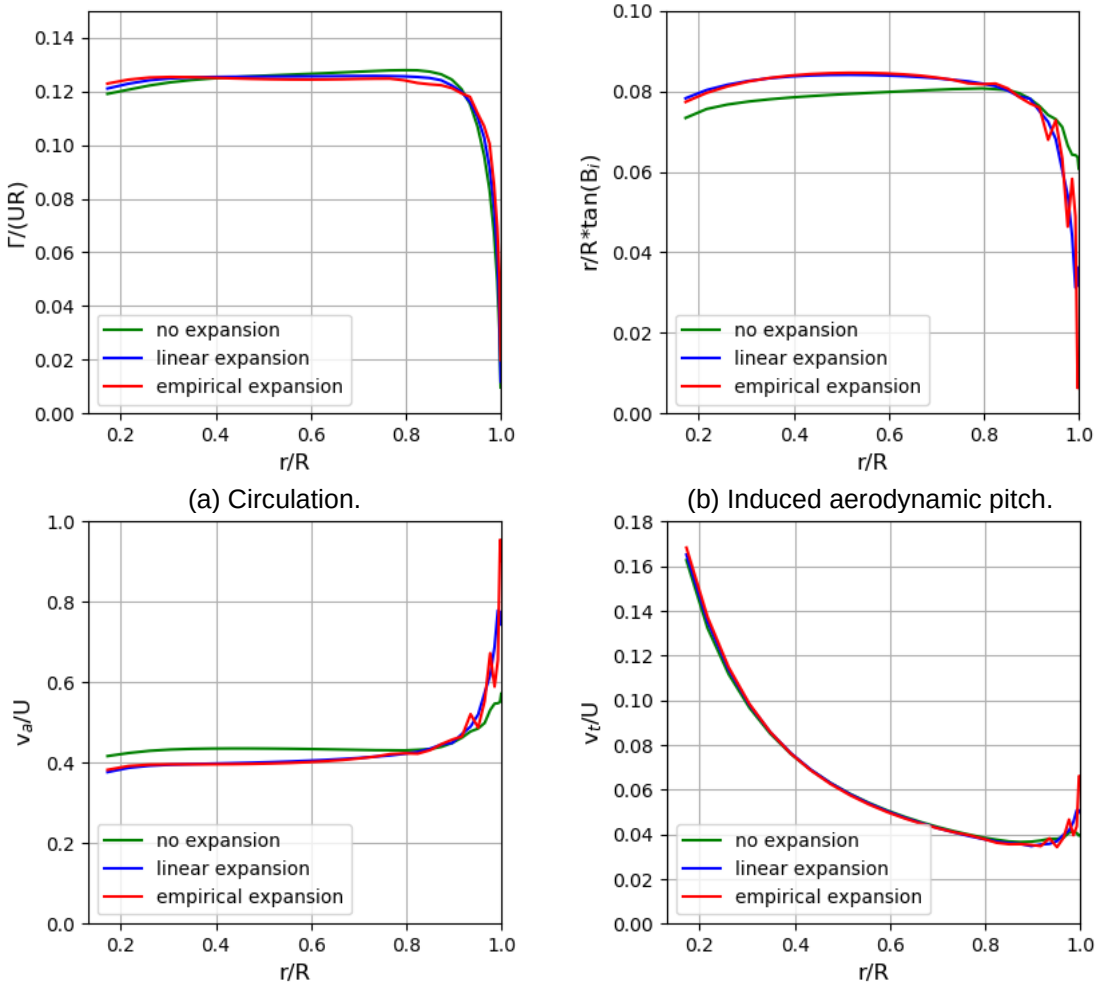

(a) Circulation.

(b) Induced aerodynamic pitch.

(c) Induced axial velocity.

(d) Induced tangential velocity.

Figure 4.7: Comparison of local variables distributions obtained with and without the wake expansion

In Figure 4.7a we can see that in all three cases the value of the circulation goes to zero as we approach the blade tip, what is a desired result. The circulation and induced tangential velocity distributions in the case without the wake expansion are like in the case with the effect of the expansion. When it comes to the induced axial velocity (Figure 4.4b), it is higher for the case without the wake expansion along almost whole lifting line span, except the tip region. This into the distribution plotted in the Figure 4.7c, as

induced aerodynamic pitch and induced axial velocity are related by Equation 2.17. The curves representing both expansion methods are overlapping in all local variables' distributions, however, in the case of the empirical function 2.34 expansion we can notice some oscillations as we approach the blade tip. It is important to mention that such (and even stronger) oscillations occur for some configurations of the input parameters, as depicted in Figure 4.8. When the numerical integration is used the computational model is very sensitive to the changes in the wake discretization parameters and thus it is exposed to higher numerical errors. Therefore, it is recommended to choose discretization parameters very carefully and to always check wake geometry to avoid oscillations that may indicate undesired numerical issues.

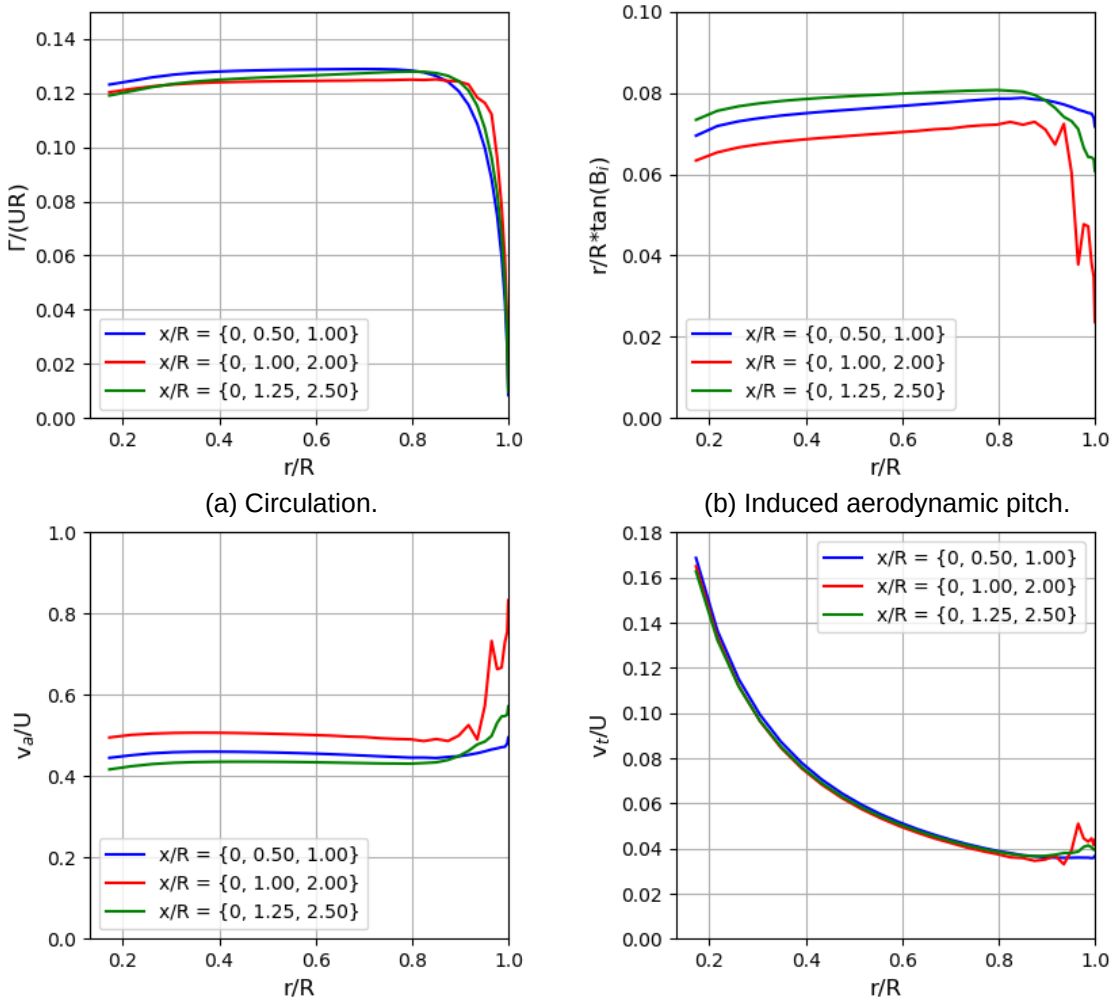

(a) Circulation.

(b) Induced aerodynamic pitch.

(c) Induced axial velocity.

(d) Induced tangential velocity.

Figure 4.8: Comparison of local variables distributions obtained without the wake expansion for different configurations of the alignment stations

4.2.2 Maximum radius of expansion

This series of tests was performed to check how the maximum radius of the expansion influences the overall performance of the computational model. The input parameters from Table 4.1 were used and the wake was aligned at three stations: $x/R = \{0, 1.25, 2.5\}$ as for this configuration the wake geometry was smooth in the case without the wake expansion. In every consecutive test the wake was expanded more, starting from the case without the wake expansion and ending at fully expanded wake with radius $r_{max}/R = 1.27$ (resulting from Equation 2.32 for the imposed load $C_{T_0} = 0.8$). Note, that in this analysis the maximum radius of expansion is imposed in each test, not directly coupled with the imposed load. Tests were repeated for both expansion methods. The values of the power coefficients for all ten tests are presented in Figure 4.9.

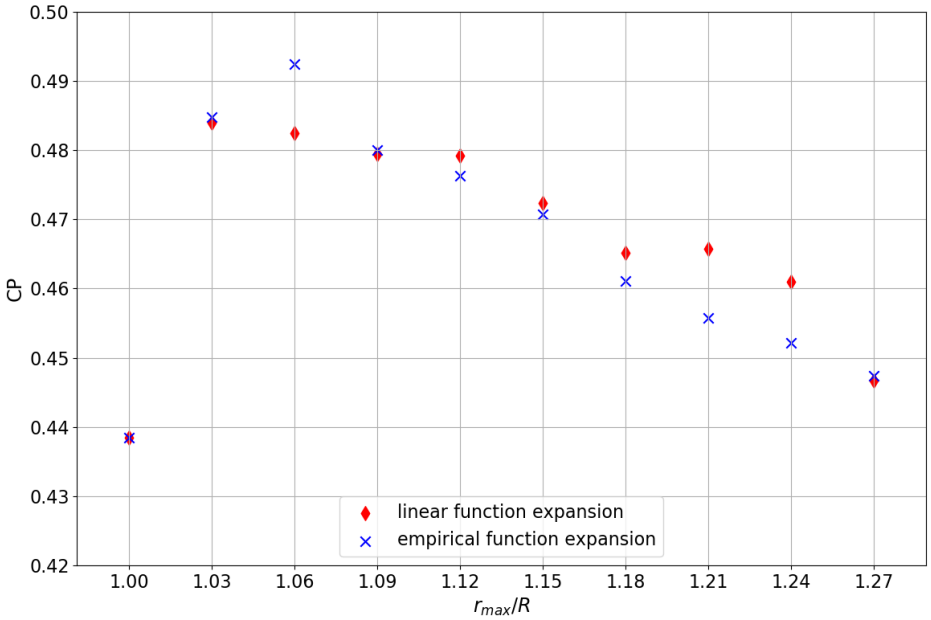

Figure 4.9: The power coefficient for increasing maximum radius of the expansion

In Figure 4.9 we can notice how with the increase of the maximum radius of the expansion (from $r_{max}/R = 1.03$ to $r_{max}/R = 1.27$) the value of the power coefficient gradually decreases. This effect is common for both expansion methods. What is very interesting and hard to explain, is the value of the power coefficient for the case without the wake expansion (i.e. for $r_{max}/R = 1.00$) which is much lower than in any of the cases with the expansion. It seems, that introduction of even small expansion effect causes sudden rise of the power coefficient. This behavior is strange, because the introduction of the wake expansion only influences the wake geometry, not the equations responsible for solving the system of equations nor formulas used to compute the value of C_P. Thus, we could expect a slow change of the power coefficient with the gradual increase of the maximum expansion radius. However, at this stage of the research, there is no reason to use different radius of the expanded wake than the one that can be calculated using Equation 2.32, so this approach is recommended.

4.3 Parametric studies

Up to this point we have been checking the effect of changing the parameters of the computational model itself. Now, we will focus on the influence of design parameters such as tip speed ratio λ and drag-to-lift ratio ε on the solution of the model with fixed settings. The values of remaining input parameters will be as listed in Table 4.1. Note, that in case of three alignment stations we will use configurations recommended in Section 4.2.1: $x/R = \{0, 1.25, 2.5\}$ for tests without the wake expansion and $x/R = \{0, 1, 2\}$ for tests with the wake expansion.

Tip Speed Ratio

In the first parametric study we check how the power coefficient is affected by increasing value of the tip speed ratio, which according to Equation 2.16 is the ratio between the blade tip velocity and the velocity of the incoming flow. Tests were repeated with and without the consideration of the viscous effects. What is important, as we are analyzing the design problem, results do not present the preformance of a certain turbine under changing conditions but show the performace expected from turbines optimized for a range of the tip speed ratio values with the imposed load $C_{T_0} = 0.8$.

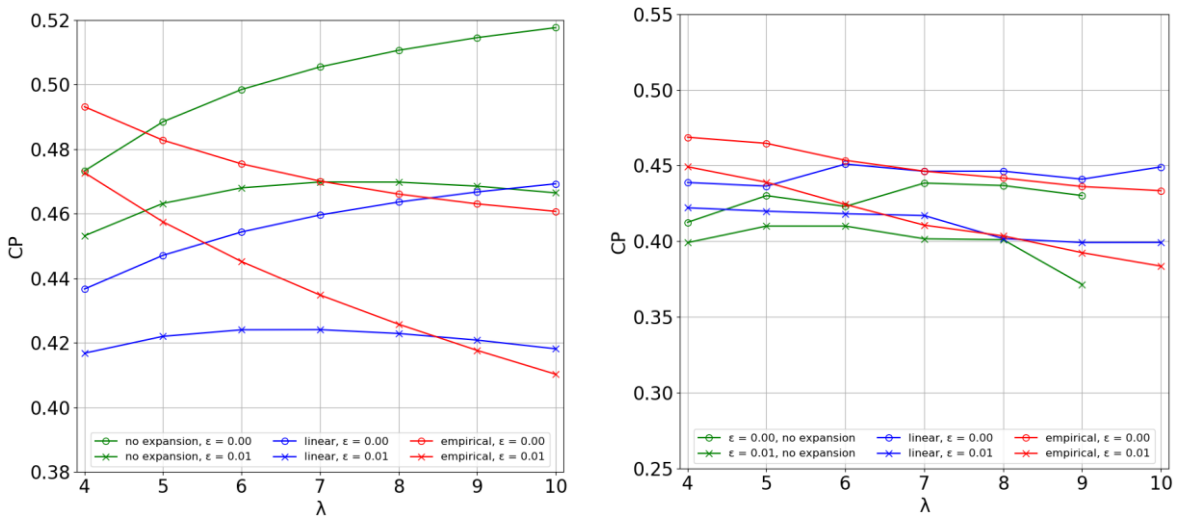

(a) Wake aligned at the lifting line. (b) Wake aligned at three stations.

Figure 4.10: Effect of the tip speed ratio on the power coefficient

The figure 4.10a shows how the power coefficient changes for the increasing value of the tip speed ratio when the wake is aligned only at the lifting line. The curves representing cases without the expansion and with the linear expansion show the known and expected result: a monotonic increase of the power coefficient with rising value of the tip speed ratio, described in detail by Sousa [29]. The interesting fact is that application of the wake expansion significantly decreases the value of the power coefficient predicted by the model. When the effect of drag is included at some point the viscous losses contribute to the noticeable decrease of the power coefficient and considering higher tip speed ratios no longer bring a benefit to the expected turbine performance.

For tests with the use of the empirical expansion function 2.34 we see an unexpected result: the value of the power coefficient is decreasing with the increasing tip speed ratio. This behavior is difficult to explain and may indicate that the geometry defined using this approach is not realistic, as the slope of the function proposed by Hoshino (given by Equation 2.34 and depicted in Figure 2.5) is very steep in the vicinity the lifting line.

Figure 4.10b presents results in the case of three alignment stations. Here, the influence of the increasing design tip speed ratio is not as apparent as in case from Figure 4.10a. The reason for that may be much more complex geometry of the vortex sheet compared to the case with the wake aligned only at the lifting line in which each trailing vortex is a helicoidal line. When the wake is aligned at multiple stations its geometry changes rapidly in the transition zone and the local variables, due to numerical instabilities, are more likely to be subject to the undesired oscillations. This may be further reflected in the value of the power coefficient, which, according to Equation 3.26, depend on distributions of the circulation and induced axial velocity over the lifting line.

Drag-to-Lift Ratio

Next, the influence of different drag-to-lift ratio was tested. For each of three considered approaches to the wake expansion was tested for several values of the drag-to-lift ratio from $\varepsilon = 0$ to $\varepsilon = 0.05$. The results of the study are presented in Figure 4.11.

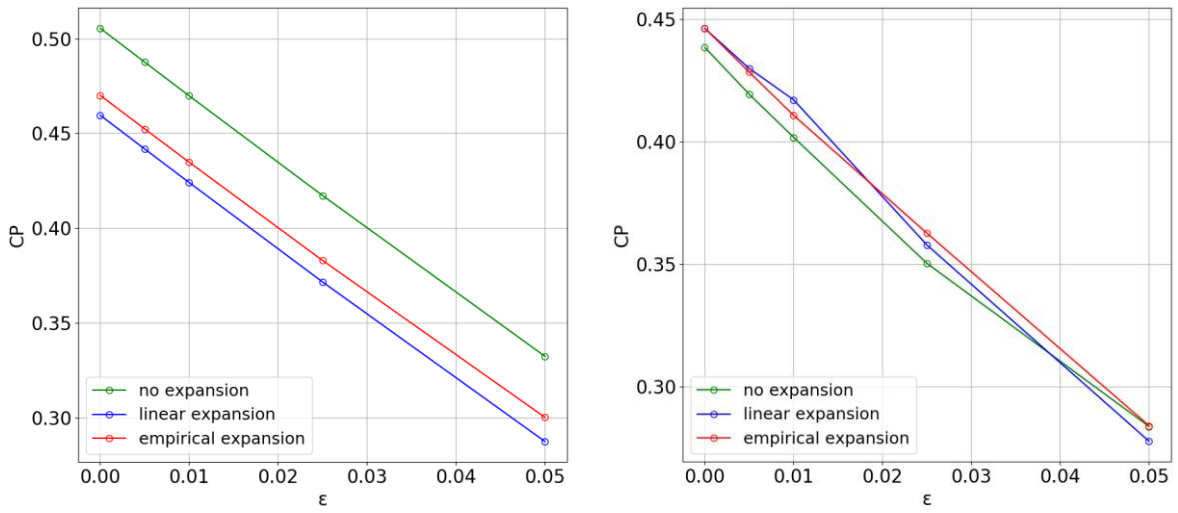

(a) Wake aligned at the lifting line.

(b) Wake aligned at three stations.

Figure 4.11: Effect of the drag-to-lift ratio on the power coefficient

The decrease of the power coefficient is almost linear with rising drag-to-lift ratio. This result was also obtained and discussed by Sousa, however, with the application of the Lerbs' analytical expressions, not the numerical approach. In Figure 4.11a we can see that the introduction of the wake expansion contributes to the decrease of the power coefficient. On the other hand, in case of three alignment stations (Figure 4.11b) we observe the opposite behavior: for most of tested values of drag-to-lift ratio the value of the power coefficient is higher when the expansion procedure is applied. Moreover, due to aforementioned numerical instabilities, characteristics obtained for multiple alignment stations are not perfectly linear.

5 Conclusions

In this thesis we implemented the wake expansion to the wind turbine design procedure of the lifting line model. The approaches to the wake expansion, together with the relevant theory as well as the details of its practical application were discussed in the consecutive chapters.

Most of analyzed aspects were before covered by Sousa [29] – without the effect of the wake expansion and with the use of an analytical approach. The application of the wake expansion, as well as the wake alignment, assumes variable wake geometry in the region of the transition wake. This excludes the use of Lerbs' analytical expressions that can only be applied to the perfectly helicoidal wakes. Therefore, in this work we have been focused fully on the application of numerical approach which requires the considerations of the vortex sheet discretization and the numerical integration.

We started with the convergence analysis in which we tested how the choice of the input parameters responsible for the wake discretization influences the overall convergence of the model with the considerations of the wake expansion. At this point, it is crucial to remember that numerical methods are subject to errors and uncertainties, and our model inevitably suffer from them too. For example, in the case of the convergence analysis for increasing discretization of the lifting line the numerical instabilities apparently exceeded the contribution coming from the change of tested model parameter, so that it was difficult to draw new and meaningful conclusions. Moreover, the disturbances were more pronounced when the wake was aligned at multiple stations. Therefore, we decided to use the wake discretization parameters recommended by Sousa [29] as the ones giving sufficient accuracy for a reasonable computational cost.

Next, the parameters of the transition wake were analyzed. This part is of vast importance, as in transition region the two most important features of our code play a main role, namely the wake alignment, and the wake expansion. We tested how the number and the configuration of the alignment stations influence the wake behavior and the expected turbine performance. The most remarkable conclusion that can be drawn from this study is that input parameters should be chosen carefully for the specific design case. For instance, the set of the input parameters which give satisfactory results in the case with the wake expansion does not necessarily work well when we assume a cylindrical wake. The model is very sensitive to the changes of parameters defining the wake geometry. It is recommended to always aim at smooth wake geometries by inspection of the local variables' distributions and visual inspection of the vortex sheet shape. Any oscillations caused by the numerical issues are unwelcome and can lead to inaccurate values of the power coefficient.

An interesting remark is that in analyzed cases with two and three alignment stations the introduction of the wake expansion procedure contributed to slightly reduced but more stable and repeatable values of the power coefficient. Moreover, the number of the alignment stations seem to have stronger impact on the expected turbine performance than the position of the last of them (i.e. the length of the transition zone).

The next test revealed that the value of the power coefficient decreases with the increase of the maximum radius of the expansion. The interesting fact that is hard to justify, is the sudden increase of the value of the power coefficient immediately after the wake expansion procedure is applied (even for very small maximum expansion radius $r_{max}/R = 1.03$ – see Figure 4.9).

When we finally move to the parametric studies, we must notice that, like in the case of the convergence analysis, the introduction of the numerical approach and the multiple wake alignment stations reduces the readability of the results. In the tests with only one alignment station we could observe well known dependency of the power coefficient on the value of the design tip speed ratio, discussed by Sousa [29]. However, in the tests with three alignment stations the obtained data is difficult to interpret – once again the model shows a high sensitivity to the disturbances caused by numerical issues.

Unfortunately, in case of the expansion with the function adapted from Hoshino we face results which are not coherent with the known research (e.g. $C_P.(\lambda)$ characteristic from Figure 4.9a). There may be several reasons why we observe such unexpected behavior. First, we need to keep in mind that the function proposed by Hoshino was originally developed to model the contraction of the wake in considerations of the marine propellers. For our research, we adapted the function without introducing any adjustments, that could contribute to the improvement of the results of the procedure in which this function is used for the wake expansion. Secondly, the empirical function 2.34 is characterized by a very steep slope in the vicinity of the lifting line (see Figure 2.5). This may hypothetically be a source of the numerical problems, as it causes rapid radial stretching of the wake geometry which in this region is already subject to strong variations.

Summarizing, we can speculate that the more realistic shape of the expansion function lies somewhere between the linear function and the function adapted from Hoshino – i.e. between lines at the graph from Figure 2.5. Note, that in this thesis we considered just two chosen functions for defining the geometry of the transition wake expansion and the radial induced velocities were not computed.

There is certainly a lot of room for further improvement of the lifting line code in terms of the wake expansion procedure. First, the additional detailed analysis of the possible expansion functions could lead to finding methods that give more stable and satisfying results. Even more promising approach would be the inclusion of the radial induced velocities in the wake expansion computational procedure, as it would contribute to more realistic geometry of the expanded wakes and open the door for the exploration of the roll-up effect. However, implementation of this aspect will inevitably require solving many problems of numerical and programming nature. Moreover, with the development of the additional features, we expect higher computational costs, which are already significantly increased, just due to the application of the wake alignment scheme. Here we enter the other area that could be improved, i.e. the numerical procedure itself. Finding more efficient numerical methods could help to achieve higher stability and allow us to decrease the numerical tolerance in order to obtain more accurate results.

References

[1] Theodore von Karman. Aerodynamics: Selected Topics in the Light of Their Historical Development. 2004. ISBN 0486434850.

[2] H. Helmholtz. Über Integrale der hydrodynamischen Gleichungen, welche den Wirbelbewegungen entsprechen. Journal für die reine und angewandte Mathematik, 55:25–55, 1858.

[3] Lighthill, J., & Berger, S. A. An Informal Introduction to Theoretical Fluid Mechanics. Physics Today, 41(6), 84–86, 2008. https://doi.org/10.1063/1.2811466

[4] Prandtl, L. Tragflügeltheorie. Königliche Gesellscahft der Wissenschaften zu Göttingen. 1918.

[5] A. Betz. Schraubenpropeller mit gerinstem Energieverlust. Nachristen von der Königlichen Gesellschaft der Wissenschaften zu Göttingen, pages 193–217, 1919.

[6] S. Goldstein. On the Vortex Theory of Screw Propellers. Proceedings of the Royal Society, Series A (123):440–465, 1929.

[7] H. W. Lerbs. Moderately Loaded Propellers with Finite Number of Blades and an Arbitrary Distribution of Circulation. Trans. SNAME, 60:73–129, 1952.

[8] S. Kawada. On the Induced Velocity and Characteristics of a Propeller. Journal of the Faculty of Engineering, 20, 1933.

[9] H. Maekawa. Optimum Design Method of Horizontal.axis Turbine Blades based on Lifting-line Theory. Bulletin of JSME, 29(256):3403–3408, 1986.

[10] J. Kerwin, W. Coney, and C. Hsin. Optimum Circulation Distributions for Single and Multi-Component Propulsors. In Twenty-First American Towing Tank Conference, pages 53–62, 1986.

[11] W. Coney. A Method for the Design of a Class of Optimum Marine Propulsors. PhD thesis, MIT, Cambridge, M.A., 1989.

[12] C. N. Adkins and R. H. Liebeck. Design of Optimum Propellers. Journal of Propulsion and Power, 10(5):676–682, 1994.

[13] J. J. Chattot. Optimization of Wind Turbines Using Helicoidal Vortex Model. Journal of Solar Energy Engineering, 125(4):418, 2003. ISSN 01996231. doi: 10.1115/1.1621675.

[14] S. A. Kinnas, W. Xu, Y.-H. Yu, and L. He. Computational Methods for the Design and Prediction of Performance of Tidal Turbines. Journal of Offshore Mechanics and Arctic Engineering, 134 (011101):1–10, 2012. ISSN 08927219. doi: 10.1115/1.4003390.

[15] D. M. Arán. Hydrodynamic Optimization and Design of Marine Current Turbines and Propellers. MSc Thesis in Civil Engineering, University of Texas, Austin, 2013.

[16] G. Diniz and S. Brizzolara. Fully Numerical Lifting Line Method for Optimum Propeller Design Design. In Fourth International Symposium of Marine Propellers, Austin, 2015.

[17] B. Yim. Optimum Propellers with Cavity-Drag and Frictional-Drag Effects. Journal of Ship Research, 20(2):118–123, 1976.

[18] B. Epps. OpenProp v2.4 Theory Document, 2010. ISSN 1096-9101.

[19] B. Epps, M. Stanway, and R. Kimball. OpenProp: An Open-source Design Tool for Propellers and Turbines, 2009.

[20] B. Epps. On the Rotor Lifting Line Wake Model. Journal of Ship Production and Design, 32(3): 1–15, 2016. ISSN 21582874. doi: 10.5957/JSPD.32.3.150035.

[21] B. P. Epps and R. W. Kimball. Unified Rotor Lifting Line Theory. Journal of Ship Research, 57(4): 181–201, 2013. ISSN 00224502. doi: 10.5957/JOSR.57.4.110040.

[22] R. Duarte. Estudos sobre um Método de Elementos de Fronteira para o Cálculo do Escoamento Potencial Estacionário em Hélices Propulsores Marítimos. MSc Thesis in Mechanical Engineering, Instituto Superior Técnico, Universidade de Lisboa, 1997.

[23] R. Duarte and J. Falcão De Campos. Projecto Hidrodinâmico de Hélices Propulsores com um Método Numérico de Linha Sustentadora. V Encontro Nacional de Mecânica Computacional, 2: 895–908, 1997.

[24] J. L. Machado. Projecto Hidrodinâmico de Turbinas de Corrente Marítima de Eixo Horizontal com o Modelo da Linha Sustentadora. MSc Thesis in Mechanical Engineering, Instituto Superior Técnico, Universidade de Lisboa, 2010.

[25] J. Baltazar, J. L. Machado, and J. Falcão De Campos. Hydrodynamic Design and Analysis of Horizontal Axis Marine. In ASME 30th International Conference on Ocean, Offshore and Arctic Engineering, Rotterdam, 2011.

[26] J. M. R. Caldeira. Análise de um Modelo de Perda para o Cálculo Aerodinâmico da Turbina Eólica de Eixo Horizontal NREL / NWTC com o Método da Linha Sustentadora. MSc Thesis in Mechanical Engineering, Instituto Superior Técnico, Universidade de Lisboa, 2014.

[27] D. B. Melo. Análise de Turbinas de Eixo Horizontal com o Modelo da Linha Sustentadora. MSc Thesis in Mechanical Engineering, Instituto Superior Técnico, Universidade de Lisboa, 2016.

[28] D. B. Melo, J. Baltazar, and J. A. Falcão de Campos. A Numerical Wake Alignment Method for Horizontal Axis Wind Turbines with the Lifting Line Theory. Journal of Wind Engineering and Industrial Aerodynamics, 174(January):382–390, 2018. ISSN 01676105. doi: 10.1016/j.jweia.2018.01.028.

[29] Sousa, G. Aerodynamic Optimization of Horizontal Axis Wind Turbines Using the Lifting Line Theory. MSc Thesis in Mechanical Engineering. Instituto Superior Tecnico, 2018.

[30] Anderson, John D. Fundamentals of Aerodynamics, McGraw-Hill, Boston, 2001.

[31] J. L. Machado. Projecto Hidrodinâmico de Turbinas de Corrente Marítima de Eixo Horizontal com o Modelo da Linha Sustentadora. MSc Thesis in Mechanical Engineering, Instituto Superior Técnico, Universidade de Lisboa, 2010.

[32] J. Baltazar, J. A. Falcão de Campos. Offshore Wind Energy Lecture Notes, Instituto Superior Técnico, Universidade de Lisboa, 2019.

[33] T. Hoshino, “Hydrodynamic Analysis of Propellers in Steady Flow using a Surface Panel Method. 2nd Report: Flow Field Around Propeller.,” *Journal of The Society of Naval Architects of Japan*, vol. 166, pp. 79–92, 1989.

[34] W. Morgan and J. Wrench. Some Computational Aspects of Propeller Design. Methods in Computational Physics, 4:301–331, 1965.

[35] J. Kerwin, Lecture Notes on Hydrofoils and Propellers. MIT, Cambridge MA. 2001.

A. Geometries of the wakes without the effect of the wake expansion

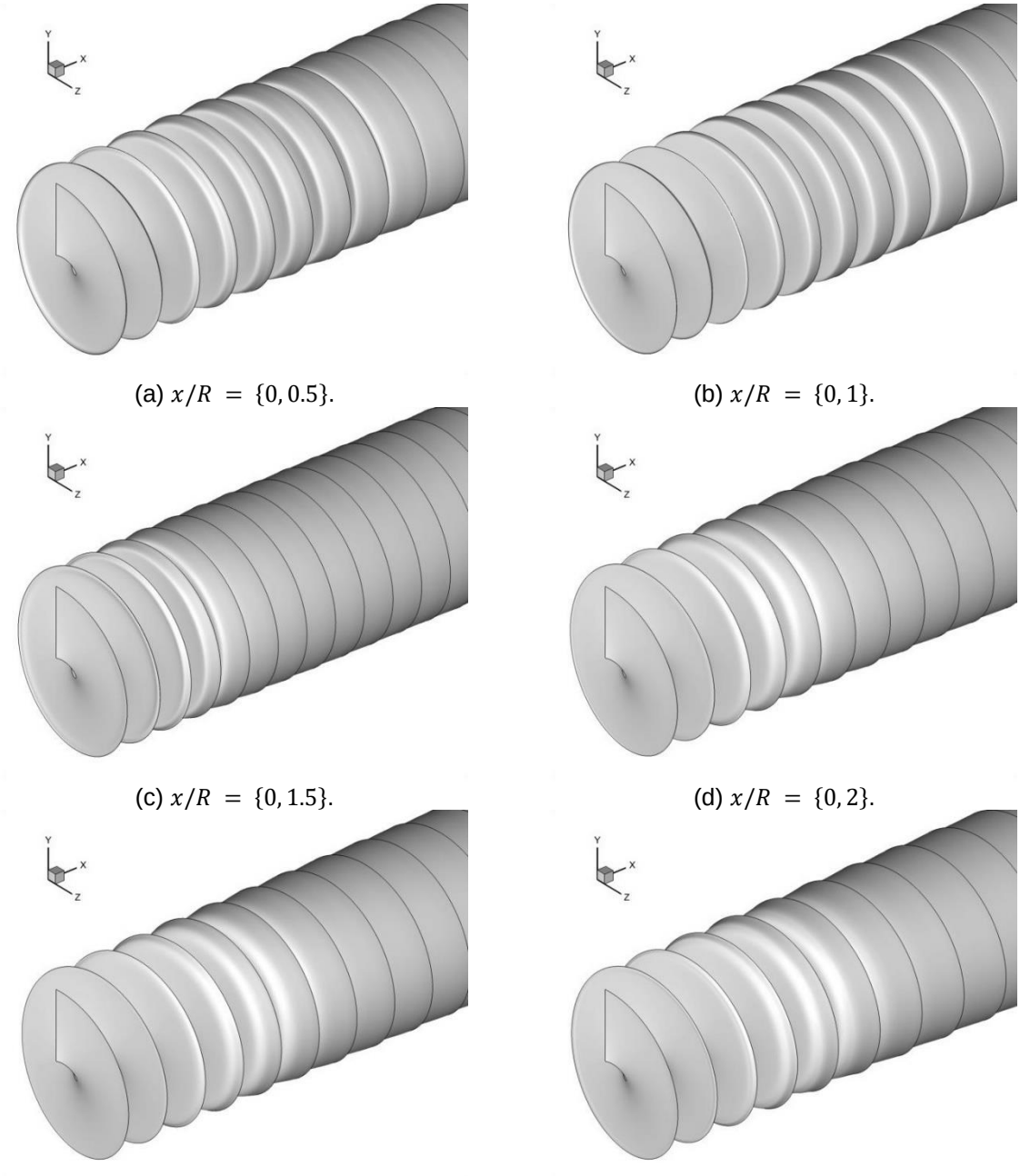

(a) $x/R = \{0, 0.5\}$.

(b) $x/R = \{0, 1\}$.

(c) $x/R = \{0, 1.5\}$.

(d) $x/R = \{0, 2\}$.

(e) $x/R = \{0, 2.5\}$.

(f) $x/R = \{0, 3\}$.

Figure A.1: Geometries of the wakes aligned at two stations – no expansion case

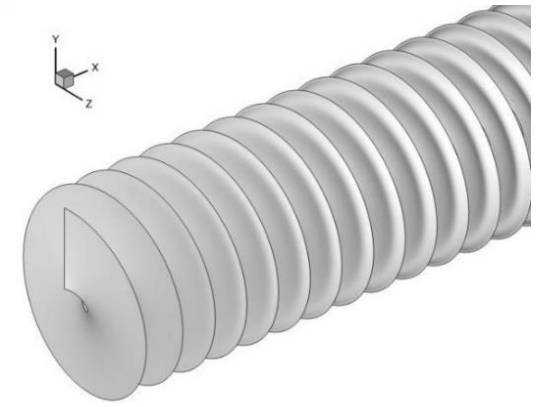

(a) $x/R = \{0, 0.5, 1\}$.

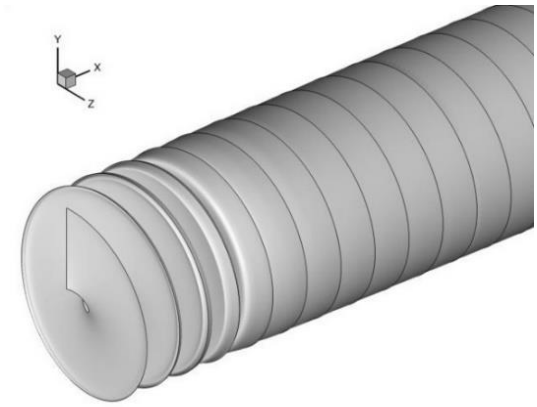

(b) $x/R = \{0, 0.75, 1.5\}$.

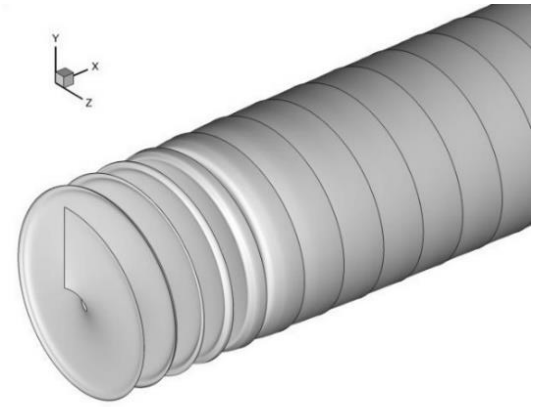

(c) $x/R = \{0, 1, 2\}$.

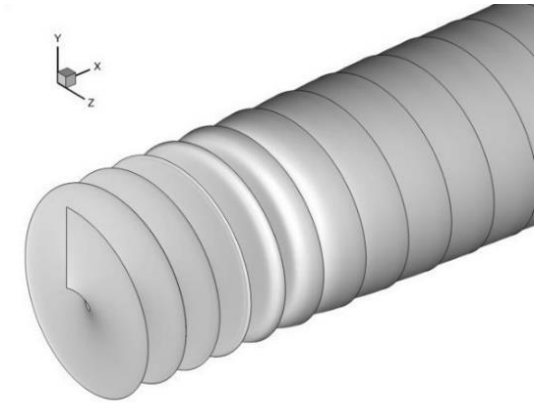

(d) $x/R = \{0, 1.25, 2.5\}$.

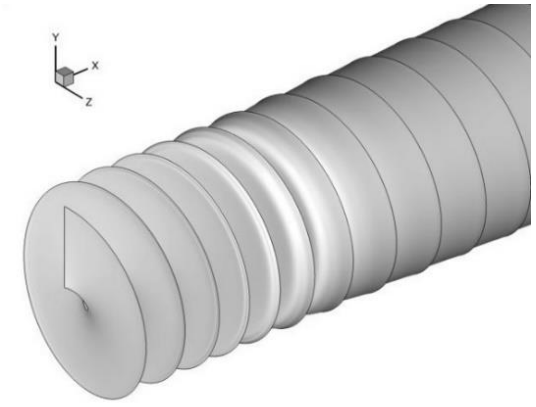

(e) $x/R = \{0, 1.5, 3\}$.

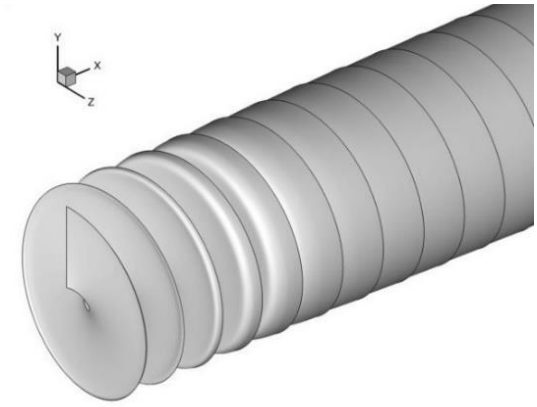

(f) $x/R = \{0, 0.25, 2\}$.

Figure A.2: Geometries of the wakes aligned at three stations – no expansion case

B. Geometries of the wakes expanded with the linear function

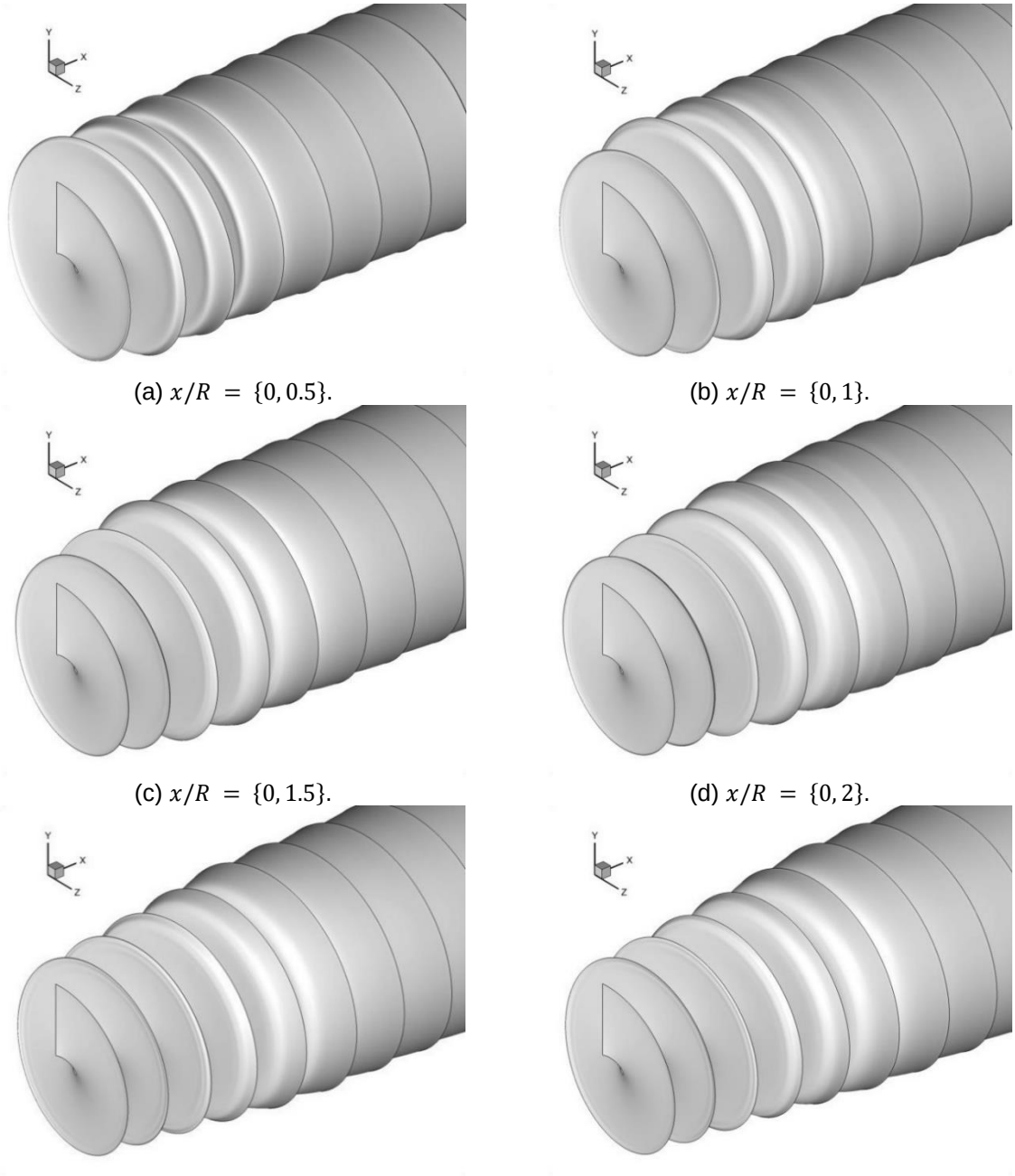

(a) $x/R = \{0, 0.5\}$. (b) $x/R = \{0, 1\}$.

(c) $x/R = \{0, 1.5\}$. (d) $x/R = \{0, 2\}$.

(e) $x/R = \{0, 2.5\}$. (f) $x/R = \{0, 3\}$.

Figure B.1: Geometries of the wakes aligned at two stations – linear expansion case

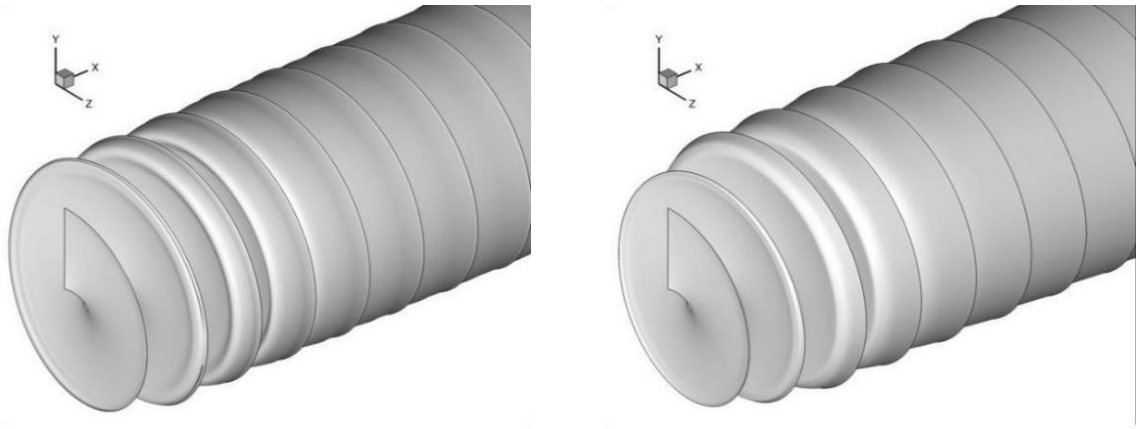

(a) $x/R = \{0, 0.25, 0.5\}$.

(b) $x/R = \{0, 0.5, 1\}$.

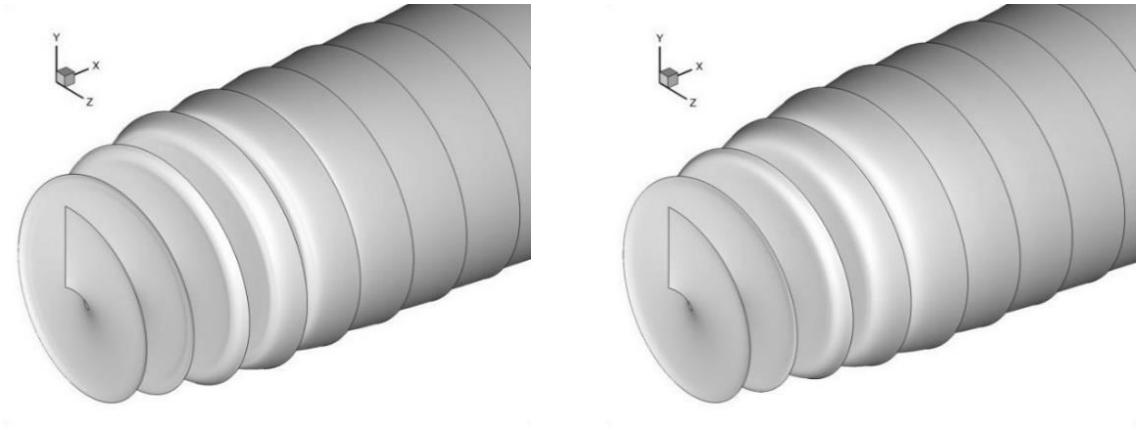

(c) $x/R = \{0, 0.75, 1.5\}$.

(d) $x/R = \{0, 1, 2\}$.

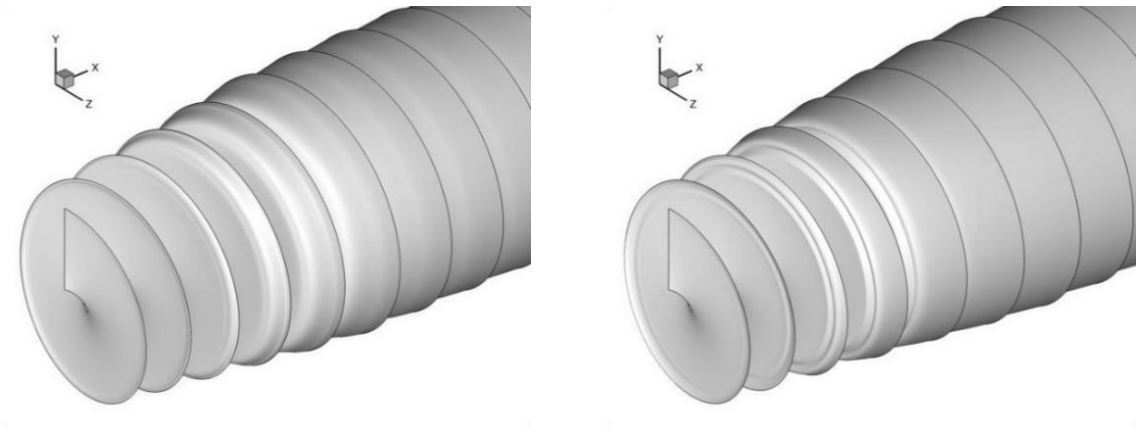

(e) $x/R = \{0, 1.25, 2.5\}$.

(f) $x/R = \{0, 1.5, 3\}$.

Figure B.2: Geometries of the wakes aligned at three stations – linear expansion case

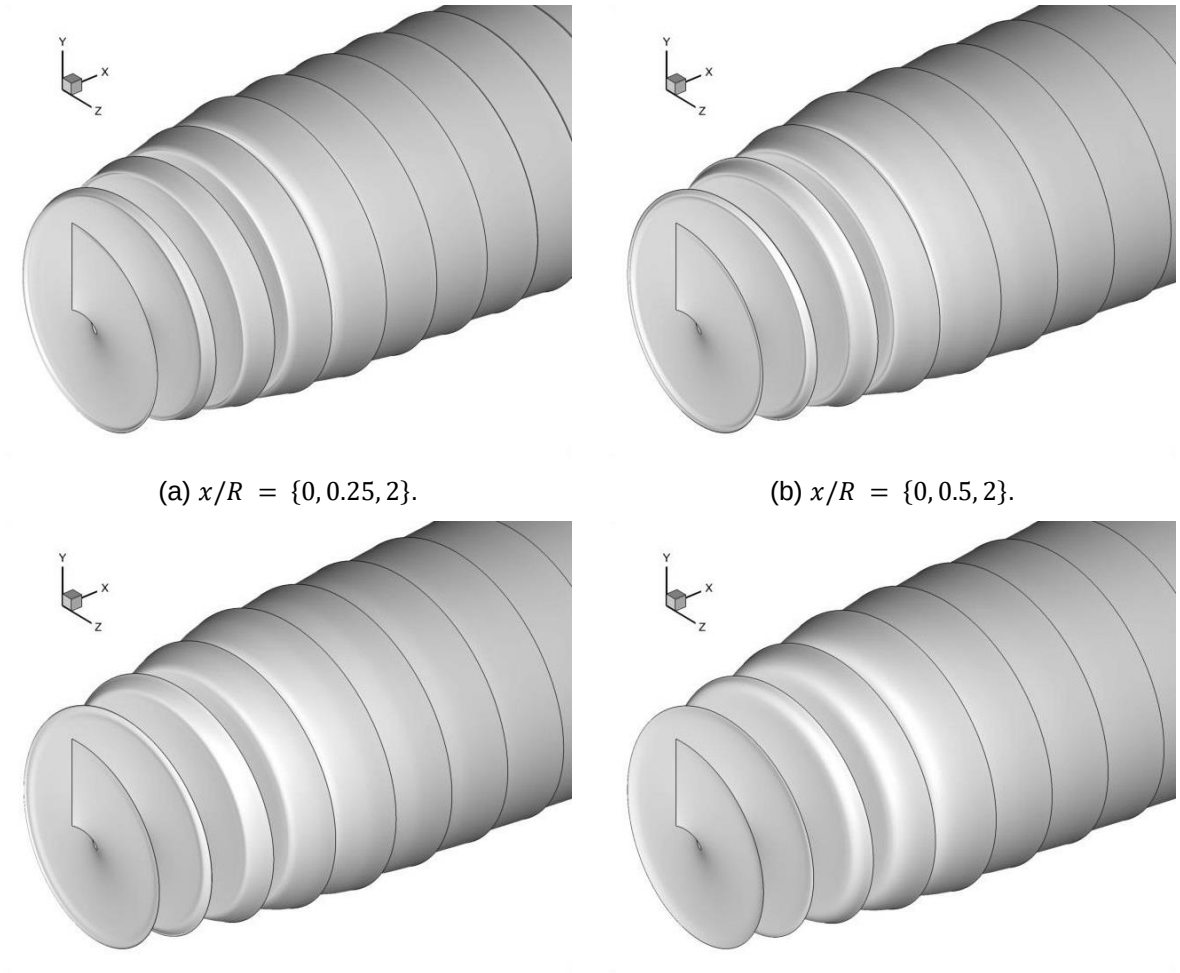

(a) $x/R = \{0, 0.25, 2\}$.

(b) $x/R = \{0, 0.5, 2\}$.

(c) $x/R = \{0, 0.75, 2\}$.

(d) $x/R = \{0, 1, 2\}$.

Figure B.3: Wakes with different position of intermediate alignment station – linear expansion case

C. Geometries of the wakes expanded with the empirical function

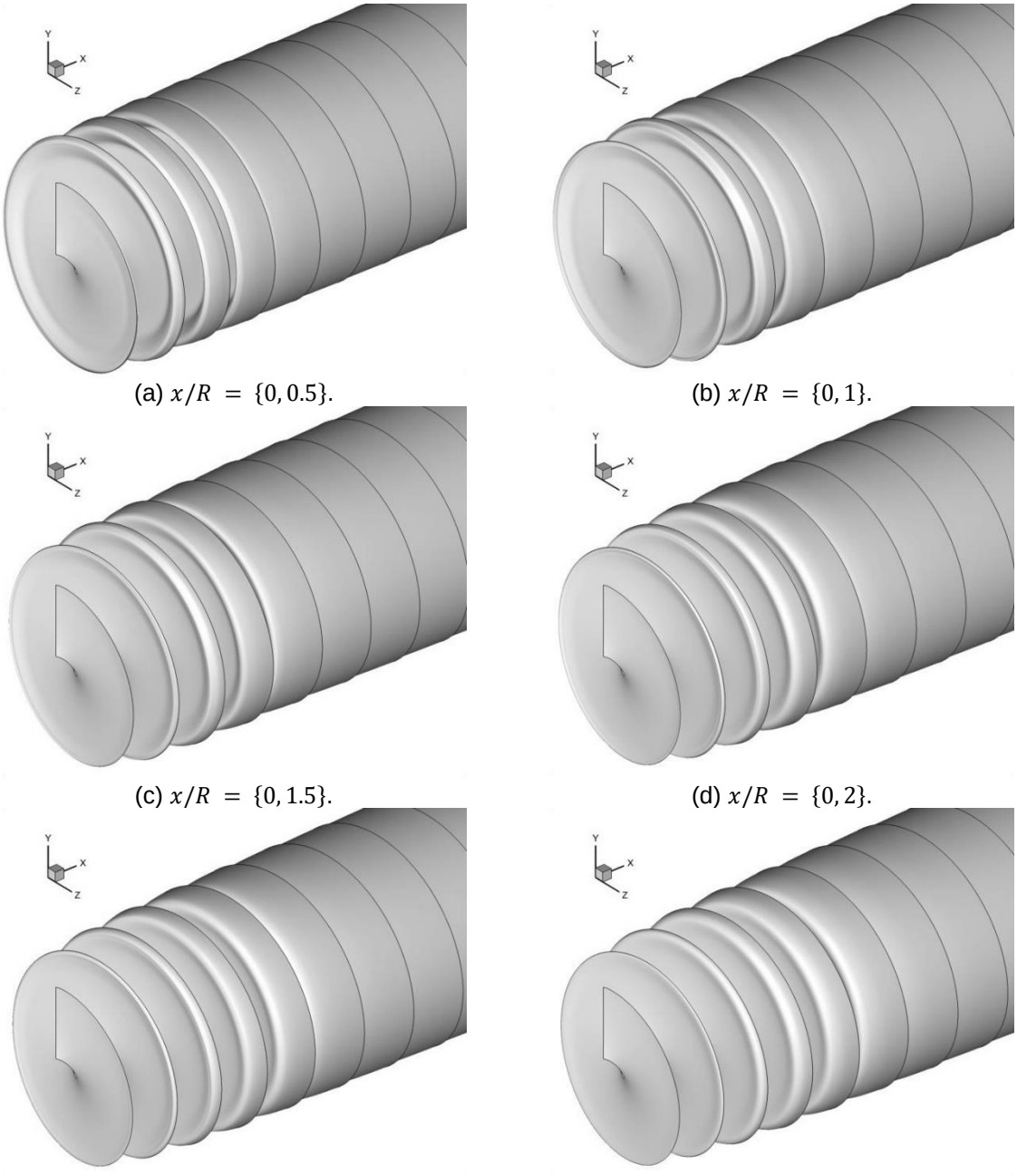

(a) $x/R = \{0, 0.5\}$. (b) $x/R = \{0, 1\}$.

(c) $x/R = \{0, 1.5\}$. (d) $x/R = \{0, 2\}$.

(e) $x/R = \{0, 2.5\}$. (f) $x/R = \{0, 3\}$.

Figure C.1: Geometries of the wakes aligned at two stations – empirical function expansion

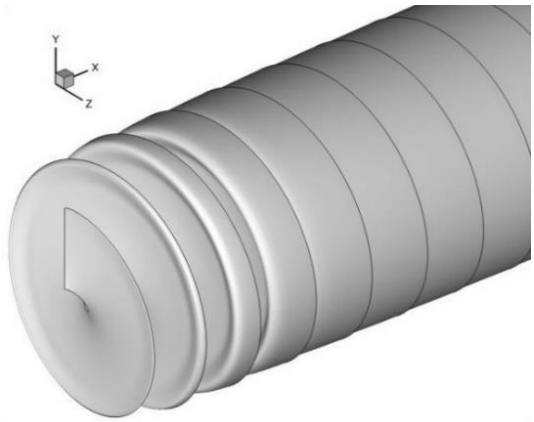

(a) $x/R = \{0, 0.5, 1\}$.

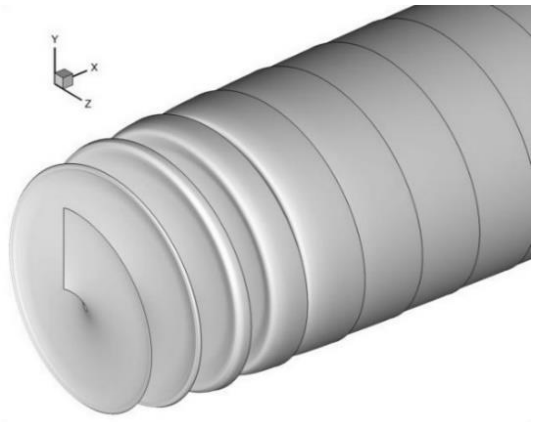

(c) $x/R = \{0, 0.75, 1.5\}$.

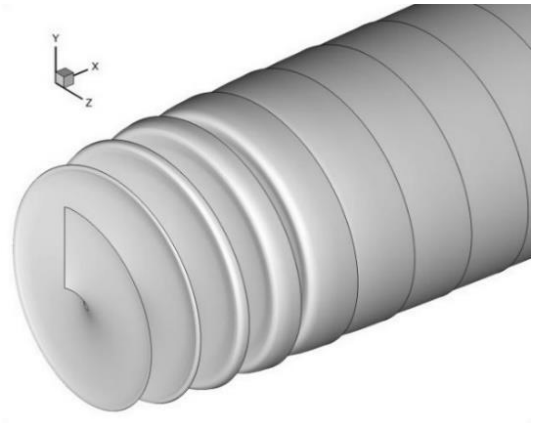

(d) $x/R = \{0, 1, 2\}$.

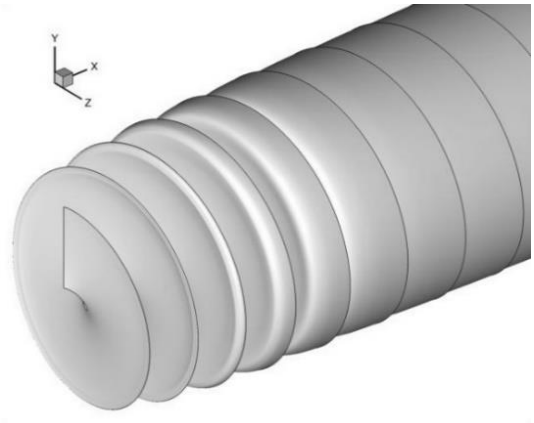

(e) $x/R = \{0, 1.25, 2.5\}$.

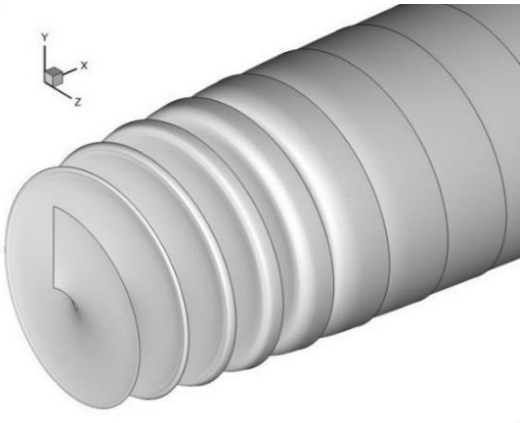

(f) $x/R = \{0, 1.5, 3\}$.

Figure C.2: Geometries of the wakes aligned at three stations – empirical function expansion

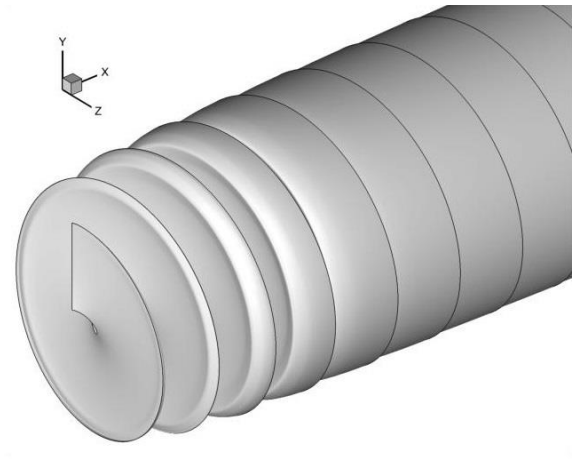

(a) $x/R = \{0, 0.25, 2\}$.

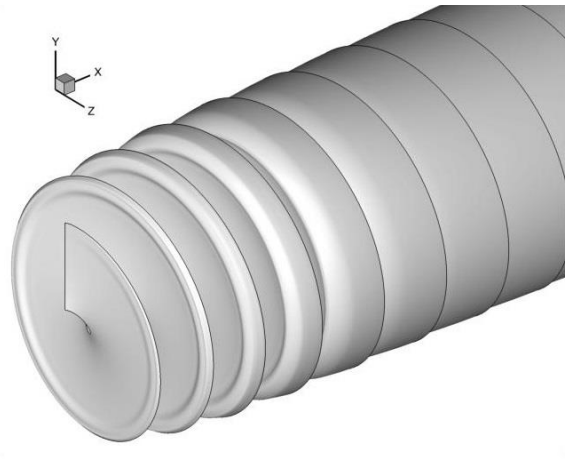

(b) $x/R = \{0, 0.5, 2\}$.

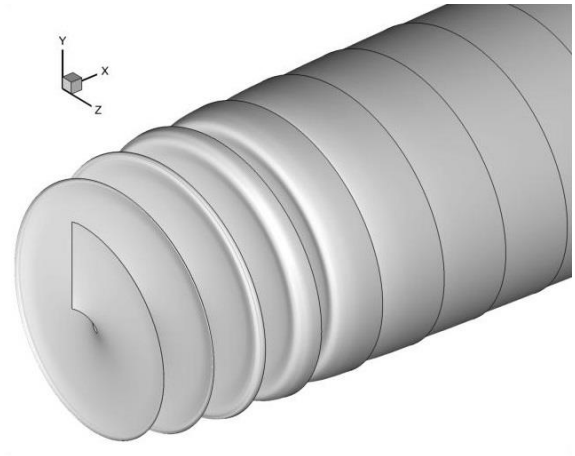

(c) $x/R = \{0, 0.75, 2\}$.

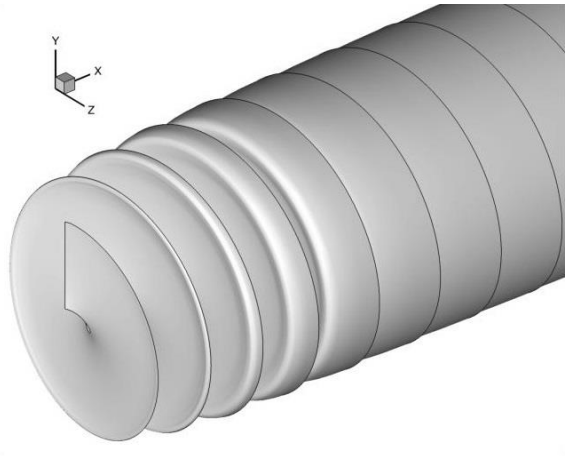

(d) $x/R = \{0, 1, 2\}$.

Figure C.3: Wakes with different intermediate alignment station position – empirical function expansion